NTNU
Norwegian University of
Science and Technology

# Simulation of Rotor-Stator Interactions (RSI's) in a High Head Francis Turbine

**Madeleine Josephine Selvig Hallén**

Master of Science in Mechanical Engineering
Submission date: June 2018
Supervisor: Ole Gunnar Dahlhaug, EPT
Co-supervisor: Chirag Trivedi, EPT

Norwegian University of Science and Technology
Department of Energy and Process Engineering

NTNU

Norwegian University
of Science and Technology

Department of Energy
and Process Engineering

EPT-M-2018-79

# MASTER THESIS

for

Student Madeleine J. Selvig
Spring 2018

***Pressure pulsations in high head Francis Turbines***
*Trykkpulsasjoner i høytrykks Francis turbiner*

**Background**

The average age of Norwegian hydro power plants are 45 year, and many show sign of fatigue and needs to be constantly maintained or refurbished. Additionally, some power plants in Norway has experienced failures on new Francis runners: Driva-, Sønnå-, Svartisen-, Hol 1-, and Vinje Power Plant. The main problem is the formation of cracks in the turbine runner.

The challenges for the numerical analysis of the Fluid-Structure Interaction (FSI) on high head Francis turbines originates in the natural frequency of the turbine runner and the fluid properties of the existing pressure oscillations.

Recently, researchers in the Waterpower Laboratory at the Norwegian University of Science and Technology, (NTNU) designed their own High head Francis turbine and published both geometry and model performance data in order to provide other researchers with a relevant case to work with and to promote the Francis-99 workshops. The Francis-99 workshops aim to determine the state of the art of high head Francis turbine simulations (flow and structure) under steady and transient operating conditions as well as promote their development and knowledge dissemination openly. This project will provide some of the necessary knowledge to understand how to carry out measurements of the stresses on the turbine runner blades.

**Objectives**

Find the pressure pulsations from a CFD-analysis of a Francis turbine runner and compare the result with existing experimental data.

**The following tasks are to be considered:**

1. Literature study
    - Pressure pulsations on a Francis turbines
    - Understand how the experimental measurements was carried out on the Francis turbine in the Waterpower Laboratory
2. Software knowledge
    - CFD analysis by ANSYS
    - Calculation of frequencies from pressure pulsations by ANSYS
3. Carry out CFD-analysis on the Francis turbine runner for minimum 10 selected operation loads of the hill diagram of a Francis turbine.
4. If the student will go to Nepal for a excursion, earlier and further work will be presented as a publication and presented at the conference; 8$^{th}$ *International symposium on Current Research in Hydraulic Turbines (CRHT-VIII)* at Kathmandu University in March 2018.
5. If there is time available, the student shall join the pressure- and efficiency-measurement for selected parts of the hill diagram of the Francis turbine in the Waterpower Laboratory.

Within 14 days of receiving the written text on the master thesis, the candidate shall submit a research plan for his project to the department.

When the thesis is evaluated, emphasis is put on processing of the results, and that they are presented in tabular and/or graphic form in a clear manner, and that they are analyzed carefully.

The thesis should be formulated as a research report with summary both in English and Norwegian, conclusion, literature references, table of contents etc. During the preparation of the text, the candidate should make an effort to produce a well-structured and easily readable report. In order to ease the evaluation of the thesis, it is important that the cross-references are correct. In the making of the report, strong emphasis should be placed on both a thorough discussion of the results and an orderly presentation.

The candidate is requested to initiate and keep close contact with his/her academic supervisor(s) throughout the working period. The candidate must follow the rules and regulations of NTNU as well as passive directions given by the Department of Energy and Process Engineering.

Risk assessment of the candidate's work shall be carried out according to the department's procedures. The risk assessment must be documented and included as part of the final report. Events related to the candidate's work adversely affecting the health, safety or security, must be documented and included as part of the final report. If the documentation on risk assessment represents a large number of pages, the full version is to be submitted electronically to the supervisor and an excerpt is included in the report.

Pursuant to “Regulations concerning the supplementary provisions to the technology study program/Master of Science” at NTNU §20, the Department reserves the permission to utilize all the results and data for teaching and research purposes as well as in future publications.

The final report is to be submitted digitally in DAIM. An executive summary of the thesis including title, student’s name, supervisor's name, year, department name, and NTNU's logo and name, shall be submitted to the department as a separate pdf file. Based on an agreement with the supervisor, the final report and other material and documents may be given to the supervisor in digital format.

☒ Work to be done in the Waterpower laboratory
☐ Field work

Department of Energy and Process Engineering, 15. January 2017

Ole G. Dahlhaug

Ole Gunnar Dahlhaug
Academic Supervisor

Co-Supervisors:

- Chirag Trivedi

Master thesis

# Simulation of Rotor-Stator Interactions (RSI's) in a High Head Francis Turbine

Madeleine J. Selvig Hallén

**Norwegian University of Science and Technology**

**Department of Energy and Process Engineering**

# Abstract

As energy demand is growing along with the quest for green energy the operating range for hydropower is being pushed into non-favourable conditions. The unsteady flow regimes at these conditions lead to transient phenomenons like pressure oscillations that can propagate through the whole turbine, threatening the reliability of the turbine. It is therefore important to identify these pressure pulsations to ensure safe operation. This master thesis presents transient simulations of the Francis model turbine at the Waterpower Laboratory at NTNU for eleven different guide vane openings ranging from a 4-degree opening to a 14-degree opening. The software used for the simulations is ANSYS CFX 18.1, applying the SST turbulence model. The primary focus is Rotor-Stator Interactions (RSI's), hence the model has been simplified accordingly, limiting the computational domain to guide vanes, runner and part of the draft tube. The frequency spectrum for pressure fluctuations have been obtained at several monitor points in the domain through Fast Fourier Transformations (FFT) using MATLAB, and then compared to experimental values for validation. The frequencies for RSI's are quite accurately predicted and it is possible to identify the trends for the amplitudes when considering the pressure pulsations in a single point at different guide vane openings. However, comparing different points in the domain at the same guide vane opening does not yield the same trend for the amplitudes for the simulations and the experiments. It is believed that this is due to differences in mesh resolution for the guide vane domain and the runner domain, but further studies need to be conducted to test this hypothesis.

(PAGE INTENTIONALLY LEFT BLANK)

# Sammendrag

Etterspørselen etter grønn energi øker, og innføring av vind- og solenergi har ført til at kravene til fleksibilitet innen vannkraft øker. Turbiner blir tvunget til å drives ved ugunstige driftspunkter, noe som fører til transiente fenomener som trykkpulsasjoner som kan forplante seg gjennom hele turbinen og true påliteligheten til turbinen. Det er derfor viktig å identifisere disse trykkpulsasjonene slik at man kan sikre trygg drift. Denne masteroppgaven presenterer transiente simuleringer av Francisturbinen på vannkraftlaboratioriet på NTNU for elleve ulike ledeskovlåpninger. Ledeskovlåpningen varier fra en 4-graders åpning til en 14-graders åpning. ANSYS CFX 18.1 med SST turbulensmodell har blitt brukt for simuleringene. Fordi hovedfokuset er på såkalte rotor-stator-interaksjoner (RSI-er), er simuleringsmodellen blitt forenklet ved å begrense domenet til å kun inkludere ledeskovler, løpehjul og den øverste delen av sugerøret.

Frekvensspekteret for trykkpulsasjoner for flere punkter i domenet er blitt beregnet ved hjelp av FFT (Fast Fourier Transformation) i MATLAB. Resultatene av simuleringene er så blitt sammenlignet med eksperimentelle målinger for verifikasjon. Frekvensene for RSI-er stemmer godt med eksperimenter, og det er mulig å identifisere trender for amplitudene når man ser på trykkpulsasjonene ved ett enkelt punkt ved ulike ledeskovlåpninger. Sammenligner man ulike punkter i domenet ved konstant ledeskovlåpning gjengir ikke simuleringene samme trend for amplitudene som eksperimentene. En teori er at dette skyldes ulikheter i oppløsningen i meshet i løpehjulet og i ledeskovlene, men denne hypotesen må testes.

(PAGE INTENTIONALLY LEFT BLANK)

# Acknowledgments

Firstly, I would like to express my sincere gratitude to my advisor, professor Ole Gunnar Dahlhaug, for your continuous support and motivation during my master thesis.

Besides my advisor, I would like to thank Chirag Trivedi and Igor Iliev for their insightful comments and encouragement.

My sincere thanks also goes to Erik Tengs, Andreas Öberg and Martin Aasved Holst – your help with the ANSYS software was invaluable. I would also like to thank the rest of the people at EDR Medeso for welcoming me into their workspace.

I thank my fellow fellow students for interesting discussions and for all the fun and frustration we shared.

Lastly I would like to thank my mother and father for your continuous support throughout my education. And thank you, dear hubby, for taking care of me and being someone I can vent to.

(PAGE INTENTIONALLY LEFT BLANK)

# Table of contents

**Abstract** **i**

**Sammendrag** **iii**

**Symbols and abbreviations** **xiii**

**1 Introduction** **1**

**2 Theory** **3**
2.1 Rotor-stator-interaction . . . . . . . . . . . . . . . . . . . . . . . . . . . . . 3
2.2 The vortex rope . . . . . . . . . . . . . . . . . . . . . . . . . . . . . . . . . 6
2.3 Vortex shedding . . . . . . . . . . . . . . . . . . . . . . . . . . . . . . . . . 6
2.4 Other fluctuations . . . . . . . . . . . . . . . . . . . . . . . . . . . . . . . . 6
2.5 Operating regimes . . . . . . . . . . . . . . . . . . . . . . . . . . . . . . . . 7
2.6 About the turbine . . . . . . . . . . . . . . . . . . . . . . . . . . . . . . . . 7
2.7 Turbulence modelling . . . . . . . . . . . . . . . . . . . . . . . . . . . . . . 8
2.8 Hill diagrams . . . . . . . . . . . . . . . . . . . . . . . . . . . . . . . . . . . 8

**3 Method** **9**
3.1 Computational domain . . . . . . . . . . . . . . . . . . . . . . . . . . . . . 9
3.2 Software and hardware . . . . . . . . . . . . . . . . . . . . . . . . . . . . . 10
3.3 Mesh . . . . . . . . . . . . . . . . . . . . . . . . . . . . . . . . . . . . . . . 10
3.4 Turbulence model . . . . . . . . . . . . . . . . . . . . . . . . . . . . . . . . 12
3.5 Simulation setup . . . . . . . . . . . . . . . . . . . . . . . . . . . . . . . . . 12
  3.5.1 Boundary conditions and initial values . . . . . . . . . . . . . . . . . 13
3.6 Steady state analysis . . . . . . . . . . . . . . . . . . . . . . . . . . . . . . 14
3.7 Transient simulations . . . . . . . . . . . . . . . . . . . . . . . . . . . . . . 14
3.8 Frequency analysis in MATLAB . . . . . . . . . . . . . . . . . . . . . . . . 14

**4 Results and discussion** **17**
4.1 Steady state results . . . . . . . . . . . . . . . . . . . . . . . . . . . . . . . 17
4.2 Transient results . . . . . . . . . . . . . . . . . . . . . . . . . . . . . . . . . 20
  4.2.1 Pressure contours . . . . . . . . . . . . . . . . . . . . . . . . . . . . . 20
  4.2.2 Frequency spectrum . . . . . . . . . . . . . . . . . . . . . . . . . . . 26
  4.2.3 Amplitudes . . . . . . . . . . . . . . . . . . . . . . . . . . . . . . . . 36

**5 Further work** **39**

**6 Conclusion** **41**

**Bibliography** **45**

**APPENDIX A: Procedures in ANSYS and MATLAB** **47**
A.1 ANSYS procedure . . . . . . . . . . . . . . . . . . . . . . . . . . . . . 47
A.1.1 ICEM . . . . . . . . . . . . . . . . . . . . . . . . . . . . . . . 47
A.1.2 CFX . . . . . . . . . . . . . . . . . . . . . . . . . . . . . . . . 47
A.2 MATLAB procedure . . . . . . . . . . . . . . . . . . . . . . . . . . . . 48

**APPENDIX B: Paper for CRHT-VIII'18** **49**

**APPENDIX C: MATLAB scripts** **65**

# List of Tables

2.1 *Table 1: Expected frequencies and diametrical modes. Based on [15] with values from [16].* . . . . 5

3.1 Mesh statistics. The number of elements in total and for each domain. . . . 11

4.1 *Comparison between measurements and simulations for torque and efficiency.* 20
4.2 *Comparison of the ratio between the first and second harmonic for simulations and experiments at location PTR2.* . . . . 28
4.3 *Comparison of the ratio between the first and second harmonic for simulations and experiments at location PTGV3.* . . . . 29
4.4 *Comparison of peak-to-peak amplitudes at PTR2, PTR4 and PTGV4.* . . . . 36

(PAGE INTENTIONALLY LEFT BLANK)

# List of Figures

2.1 2D view of the turbine model. Retrieved from [16] . . . . . . . . . . . . . . 7

3.1 An overview of the modelled flow passage. . . . . . . . . . . . . . . . . . . . . 9
3.2 Figure shows the final guide vane position during part load (left) and high load (right) when using mesh deformation. Retrieved from [24]. . . . . . . . 10
3.3 Comparison of meshes for two different alphas. . . . . . . . . . . . . . . . . . 11
3.4 Figure shows the fillet on the shroud side of the guide vane. It can be seen that the curvature is not completely smooth. This could be solved by adding more cells, but this would in return require longer simulation running time. 11
3.5 Figure shows the mesh for a main blade and a splitter blade. . . . . . . . . 11
3.6 An overview of the location of the monitor points used for simulations and analysis. . . . . . . . . . . . . . . . . . . . . . . . . . . . . . . . . . . . . 13
3.7 Representation of the sinc(x) function and the resulting side lobes. . . . . . 15

4.1 Comparison of torque between experiments and numerical results. . . . . . . 18
4.2 Comparison of efficiency between experiments and numerical results. . . . . 18
4.3 The predicted head for the simulations. . . . . . . . . . . . . . . . . . . . . . 19
4.4 Pressure contour for $\alpha = 10°$ in a stationary frame of reference. . . . . . . . 21
4.5 Pressure contour for four different alphas in a statinary frame of reference. . 21
4.6 Pressure contour for $\alpha = 10°$ in a rotating frame of reference. . . . . . . . . 22
4.7 Pressure contour for four different alphas in a rotating frame of reference. . 23
4.8 Pressure contour for the pressure side of a single main blade. . . . . . . . . 25
4.9 Pressure contour for the suction side of a single main blade. . . . . . . . . . 25
4.10 Pressure versus time for experiments and simulations. The pressure curve for the experiments has been shifted. Because of the outlet condition, the pressure in the simulations are wrongly predicted, but change in pressure is correct. . . . . . . . . . . . . . . . . . . . . . . . . . . . . . . . . . . . . . 26
4.11 Frequency spectrum for simulations at monitor point PTR2 at different alphas. 27
4.12 Frequency spectrum for experimental measurements at sensor PTR2 at different alphas. . . . . . . . . . . . . . . . . . . . . . . . . . . . . . . . . . . 27
4.13 Frequency spectrum for monitor point PTGV3 at different alphas. . . . . . 30
4.14 Frequency spectrum for experimental measurements at sensor PTGV3 at different alphas. . . . . . . . . . . . . . . . . . . . . . . . . . . . . . . . . . . 30
4.15 The interface between the mesh in the guide vanes (left side) and the mesh in the runner (right side). . . . . . . . . . . . . . . . . . . . . . . . . . . . 31
4.16 Frequency spectrum for simulations at $\alpha = 4°$ at different monitor points. . 32
4.17 Frequency spectrum for measurements at $\alpha = 4°$ at different monitor points. 32

4.18 Frequency spectrum for simulations at $\alpha = 7^\circ$ at different monitor points. . 33
4.19 Frequency spectrum for measurements at $\alpha = 7^\circ$ at different monitor points. 33
4.20 Frequency spectrum for simulations at $\alpha = 10^\circ$ at different monitor points. . 34
4.21 Frequency spectrum for measurements at $\alpha = 10^\circ$ at different monitor points. 34
4.22 Frequency spectrum for simulations at $\alpha = 14^\circ$ at different monitor points. . 35
4.23 Frequency spectrum for measurements at $\alpha = 14^\circ$ at different monitor points. 35

# Symbols and Abbreviations

| Symbol | Explanation | Unit |
|---|---|---|
| $\alpha$ | Guide vane opening | ° |
| $A_{mn}$ | Combined pressure amplitude | Pa |
| $B_m$ | Amplitude for the $m^{th}$ harmonic | Pa |
| $B_n$ | Amplitude for the $n^{th}$ harmonic | Pa |
| $\beta*$ | Closing constant | - |
| $\beta_1$ | Closing constant | - |
| $D_2$ | Outlet diameter | m |
| $\eta$ | Efficiency | - |
| $F_1$ | Function | - |
| $f_{BP}$ | Blade passing frequency | Hz |
| $f_{GV}$ | Guide vane passing frequency | Hz |
| $f_n$ | Runner rotational frequency | Hz |
| $f_R$ | Rheingan's frequency | Hz |
| $g$ | Gravity constant | $\mathrm{m/s^2}$ |
| $\gamma$ | $\gamma_1 = \beta_1/\beta * -\sigma_{\omega 1}\kappa^2/\sqrt{\beta*}$ | - |
| $H$ | Head | m |
| $k$ | Turbulent kinetic energy | J/kg |
| $\kappa$ | Closing constant | - |
| $m$ | Harmonic order | - |
| $\mu$ | Dynamic viscosity | $\mathrm{Ns/m^2}$ |
| $\mu_t$ | Turbulent viscosity | $\mathrm{Ns/m^2}$ |
| $n$ | Rotational speed | rpm |
| $n_{ed}$ | Dimensionless rotational speed | - |
| $p_s$ | Pressure in stationary field | Pa |
| $p_r$ | Pressure in rotating field | Pa |
| $t$ | Time | s |
| $\theta_s$ | Angle in stationary system | - |
| $\theta_r$ | Angle in rotating system | - |

| | | |
|---|---|---|
| $\phi_m$ | Phase for the $m^{th}$ harmonic | - |
| $\phi_n$ | Phase for the $n^{th}$ harmonic | - |
| $\omega_b$ | Runner angular speed | rad/s |
| $\omega$ | Specific turbulence dissipation rate | 1/s |
| $Q$ | Volumetric flow | $\mathrm{m}^3$/s |
| $Q_{ed}$ | Dimensionless volumetric flow | - |
| $Re$ | Reynolds number | - |
| $\sigma_k$ | Closing constant | - |
| $\sigma_\omega$ | Closing constant | - |
| $\sigma_{\omega 1}$ | Closing constant | - |
| $\sigma_{\omega 2}$ | Closing constant | - |
| $\rho$ | Density | kg/$\mathrm{m}^3$ |
| $\tau$ | Torque | Nm |
| $\tau_{ij}$ | Turbulent shear stress | Pa |
| $\nu_t$ | Eddy viscosity | $\mathrm{m}^2$/s |
| $x_k$ | Vector of N complex numbers | - |
| $y_m$ | Vector of N complex numbers | - |
| $Z_{BP}$ | Number of runner blades | - |
| $Z_{GV}$ | Number of guide vanes | - |

| Abbreviation | Explanation |
|---|---|
| BEP | Best Efficiency Point |
| CFD | Computational Fluid Dynamics |
| DES | Detached Eddy Simulation |
| FFT | Fast Fourier Transform |
| FSI | Fluid-Structure Interaction |
| GGI | General Grid Interface |
| LES | Large Eddy Simulation |
| RMS | Root Mean Square |
| RSI | Rotor-Stator Interactions |
| SNL | Speed No Load |
| SST | Shear Stress Transport |
| URANS | Unsteady Reynolds Averaged Navier Stokes |

(PAGE INTENTIONALLY LEFT BLANK)

# 1 | Introduction

Hydropower is nothing new. The first hydroelectric power plant began its operation in 1882 [1], and hydropower has been the subject of many studies. Already in 1940, Rheingan showed that the vortex rope could cause power swings and identified the so-called Rheingan's frequency [2]. Today, energy demand is growing along with the quest for green energy, and the requirement for flexibility in hydropower is being pushed to its limits. Together with frequent changes in consumption patterns from hour to hour, day to day and season to season, adjusting the energy production in real-time is becoming increasingly more important. The introduction of solar- and wind energy is driving this concept even further and the turbine is forced to operate at conditions for which it was not designed, leading to transient phenomenas like pressure pulsations that threatens the reliability of the turbine [3].

With the advancement in computer technology, Computational Fluid Dynamics (CFD) has emerged as a powerful tool for evaluating the performance of turbines. Turbines are tailor-made to specific conditions at a specific site, and small improvements in the geometry can have a large positive effect on operation [4]. Identifying problem areas is therefore very important [3].

Flow in reaction turbines is three dimensional, rotational due to the change in flow direction, turbulent and unsteady [4]. Another important attribute when looking at dynamic forces is the turbine's transient behaviour. While steady state analysis can predict efficiency, cavitation and hydraulic losses, a transient analysis is necessary in order to capture pressure pulsations [4] [3]. A characteristic of the Francis turbine is that the runner blades are fixed and cannot be adjusted to the operating conditions. The flow characteristics can be called ideal in a limited part of the operating range, i.e. close to the Best Efficiency Point (BEP), with low pressure fluctuations and high efficiency. At off-design the flow pattern is characterized by swirl, flow separation and backflow [5].

Meng et. al performed a CFD study on pressure pulsations for the complete flow passage, from the inlet of the spiral casing to the outlet of the draft tube, for an ultra-high head turbine with splitter blades. For this turbine they found that the efficiency of the turbine was the highest when the length ratio of the splitter blades was 0.75 times the length of the main blades. They also found that the amplitude of the pressure pulsations was smallest when the ratio of the splitter blades was 0.825 of the main blades [6].

Jošt and Lipej did a numerical analysis of the vortex rope and the pressure pulsations at four different operating points and compared the results with experimental data. While the frequencies they found corresponded well with experimental data, the amplitudes were less accurate. Better results for amplitudes were however obtained with a refined grid [7].

Using Detached Eddy Simulation (DES), Magnoli and Schilling numerically predicted the pressure oscillations in a complete turbine with focus on the vortex rope. The results were verified against experimental data and showed very good agreement [8]. Minakov et al. also used DES turbulence model in their simulations of a full turbine. They found that for small guide vane openings, vortices are formed in the inter-blade channels of the runner. The flow downsteam of the runner consisted of several randomly moving vortex structures. With increasing guide vane opening, the vortices only appear in a few inter-blade channels. In addition, the vortex rope was formed downstream of the runner. For large guide vane openings, there were no vortices in the inter-blade channels of the runner [9].
Yexiang et al. used Fast Fourier Transformation (FFT) on their numerical results of pressure fluctuations to identify relevant frequencies. They simulated different part load conditions, but no high load conditions. The peak-to-peak amplitudes they predicted in the spiral casing was far less for the numerical data than for the measured data [10].

For the turbine of this thesis, the model turbine installed at the Waterpower Laboratory at NTNU, Zhao Yaping et. al compared the standard k-$\epsilon$ turbulence model to the Shear Stress Transport (SST) model with different outlet boundary conditions. They found that the k-$\epsilon$ model could better predict steady state efficiency [11]. Trivedi et al. carried out experimental and numerical investigations of the whole turbine at three different loads, namely best efficiency point, high load and two different operating points at part load. The simulations took 90 days to complete, and the results showed good agreement with experiements for frequencies connected to rotor-stator interactions (RSI's) [12].

This master thesis seeks to investigate the pressure pulsations resulting from RSI's in the high head Francis turbine at the laboratory at NTNU for eleven different guide vane openings, ranging from $\alpha = 4°$ to $\alpha = 14°$, using CFD simulations. The simulations are then compared to experimental results. Seidel et al. showed that the gate passing frequency was the dominating frequency for a high head Francis unit, and that fatigue life therefore was governed nearly exclusively by RSI's [4] [13]. Hence knowledge about RSI's is especially important for high head units. Because the flow in the different turbine components are connected and interact with one another, individual component analysis does not correspond correctly to the experimental data. A full analysis on the turbine with spiral casing, distributor, runner and draft tube is necessary, according to Magnoli and Schilling [8]. Even with several simplifications, one such simulation can take weeks, or even months, depending on the computational power available. Due to the long computational time for transient CFD simulations, a simulation of the turbine as a whole was not feasible. This master thesis focuses on the interaction between the guide vanes and runner, and the domain has therefore been limited to guide vanes, runner and the draft tube cone.

Part of simulations presented in this work were conducted under the project supported by Notur/NorStore, project number-NN9504K.

# 2 | Theory

Pressure fluctuations occur naturally in hydraulic machinery and can be of a periodic or stochastic nature. According to the IEC 60193, the pulsations are influenced by machine design, operating conditions and by the dynamic response of the water conduits and rotating components. Pressure fluctuations is associated with hydro-acoustic phenomenons involving unsteady pressure and flow velocity distributions, but they can also be linked to mechanical fluctuations of shaft torque, rotational speed, hydraulic load on guide vanes etc., as well as with vibrations of the machine. Among low frequency pressure fluctuations, the draft tube surge is perhaps the most commonly identified phenomenon. Turbines also produce an excitation at the rotational frequency multiplied with the number of runner blades. Higher frequencies are generated due to the interaction of the runner blades with the guide vanes [14]. The following sections are based on the author's project thesis "Numerical simulations of rotor-stator interactions at BEP for a high head Francis turbine" [3].

## 2.1 Rotor-stator-interaction

Pressure oscillations in fluid flow is a transient phenomena that impacts the mechanical structure of the turbine. Rotor-stator-interaction (RSI) is the main source for pressure pulsations during normal operation at full load [8]. A steady state analysis is less time consuming than a transient analysis, and while it can predict performance parameters like efficiency, cavitation and hydraulic losses, analysing dynamic forces requires the calculation of unsteady flow with advanced turbulence models.

RSI results from the interaction between the rotating flow perturbations by the runner blades, and the perturbations in the flow from the guide vanes [15], thus it is associated with the blade passing frequency and guide vane frequency. The blade passing frequency $f_{BP}$, is determined by the number of runner blades, $Z_{BP}$, and the runner rotation frequency, $f_n$.

$$f_n = \frac{n}{60} \tag{2.1}$$

$$f_{BP} = f_n Z_{BP} m \tag{2.2}$$

Here $n$ is the rotational speed in rpm, $Z_{BP}$, is the number of runner blades, while m=1,2,3,... represent harmonic order. For this master thesis $n \approx 335$ rpm and $Z_{BP} = 30$, generating $f_n \approx 5.58$ Hz and $f_{BP} \approx 167.5$ Hz for the first harmonic of the blade passing frequency. The gate passing frequency, or guide vane frequency, is calculated from

$$f_{GV} = f_n Z_{GV} m \tag{2.3}$$

where $Z_{GV}$ is the number of guide vanes and m=1,2,3,... For this master thesis $Z_{GV} = 28$ and the first harmonic of the guide vane passing frequency $f_{GV} \approx 156.5$ Hz. According to Seidel et al., higher harmonics have very little impact on Francis runners [12], hence $m = 1$ is the most significant frequency.

RSI's produce pressure waves that propagate through the whole turbine. The interaction between runner and guide vanes induces pulsations at the runner inlet based on two phenomenons:

1. A rotating observer passes the wake of all guide vanes during a full rotation.
2. Every time a runner blade passes a guide vane, a pressure pulse is generated [13].

As the guide vane angle is changed, the amplitude of the frequency of the pressure pulse will vary. The most significant fluctuations arise when the trailing edge of the guide vanes are close to the runner blades. Increased distance between stator and rotor blades will increase turbulence mixing and dissipate wakes and thereby decrease RSI effects. Because low and medium head Francis units have a larger distance between rotor and stator, RSI-induced phenomenons are negligible. Pressure fluctuations caused by RSI's in the high head units are therefore most critical and can cause stability problems [13].

The flow field leaving the guide vane of a Francis turbine is characterized by the velocity irregularity caused by the guide vanes. The pressure field caused by the runner blade also induces flow field distortions. These periodic flow fields can both be represented as Fourier series, and can for the stationary and rotating pressure fields be expressed as:

$$p_s(\theta_s, t) = \sum_{n=1}^{\infty} B_n cos(n Z_{GV} \theta_s + \phi_n) \tag{2.4}$$

$$p_r(\theta_r, t) = \sum_{m=1}^{\infty} B_m cos(n Z_{BP} \theta_r + \phi_m) \tag{2.5}$$

Here, $m$ and $n$ are harmonic orders. A modulation process combines the two pressure fields into a resulting pressure field. The pressure in the vaneless gap can be expressed as the product of both the rotating and stationary pressure fields. By using the identity for circular functions and the relation between the runner angle coordinate to the stationary system of reference, $\theta_r = \theta_s - \omega t$, the pressure field in stationary coordinates becomes:

$$\begin{aligned} p_{mn} = \frac{A_{mn}}{2} cos(m Z_{BP} \omega t - (m Z_{BP} - n Z_{GV}) \theta_s + \phi_n - \phi_m) + \\ \frac{A_{mn}}{2} cos(m Z_{BP} \omega t - (m Z_{BP} + n Z_{GV}) \theta_s - \phi_n - \phi_m) \end{aligned} \tag{2.6}$$

| | | | | Stationary frame | | | Rotating frame | | |
|---|---|---|---|---|---|---|---|---|---|
| m | n | $k_1$ | $k_2$ | $\omega_1/\omega_b$ | $\omega_2/\omega_b$ | $f/f_n$ | $\omega'_1/\omega_b$ | $\omega'_2/\omega_b$ | $f/f_n$ |
| | | | | $mZ_{BP}/k_1$ | $mZ_{BP}/k_2$ | $mZ_{BP}$ | $mZ_{GV}/k_1$ | $mZ_{GV}/k_2$ | $nZ_{GV}$ |
| 1 | 1 | 2 | 58 | 15 | 0.51 | 30 | 14 | 0.48 | 28 |
| 1 | 2 | -26 | 86 | -1.15 | 0.34 | 30 | -2.15 | 0.65 | 56 |
| 2 | 2 | 4 | 116 | 15 | 0.51 | 60 | 14 | 0.48 | 56 |
| 2 | 3 | -24 | 144 | -2.5 | 0.41 | 60 | -3.5 | 0.58 | 84 |
| 3 | 3 | 6 | 174 | 15 | 0.51 | 90 | 14 | 0.48 | 84 |
| 3 | 4 | -22 | 202 | -4.09 | 0.44 | 90 | -5.09 | 0.55 | 112 |
| 4 | 4 | 8 | 232 | 15 | 0.51 | 120 | 14 | 0.48 | 112 |
| 5 | 5 | 10 | 290 | 15 | 0.51 | 150 | 14 | 0.48 | 140 |
| 13 | 1 | -2 | 782 | -195 | 0.49 | 390 | -196 | 0.50 | 392 |

*Table 2.1: Table 1: Expected frequencies and diametrical modes. Based on [15] with values from [16].*

Where m=1,2,...,∞, n=1,2,...,∞ and $\omega$ is angular speed in equation 2.6. The equation describes the pressure field in the vaneless gap. $A_{mn}$ is the combined pressure amplitude due to the interaction of each harmonics. The numbers of minima and maxima for the two diametrical pressure modes is given by:

$$k_1 = mZ_{BP} - nZ_{GV} \tag{2.7}$$

$$k_1 = mZ_{BP} + nZ_{GV} \tag{2.8}$$

with a rotational speed in the stationary frame of reference:

$$\omega_1 = \frac{mZ_{BP}\omega_b}{k_1} \tag{2.9}$$

$$\omega_2 = \frac{mZ_{BP}\omega_b}{k_2} \tag{2.10}$$

The RSI patterns are thereby determined by the relations in table 2.1 [15].

It should be mentioned that the turbine has splitter blades, which will affect the pressure pulsations from RSI. Splitter blades extend the efficiency region and decrease pressure pulsations. Meng et al. found that for an ultra-high head Francis unit with 16 main blades and 16 splitter blades, the amplitude of the blade passing frequency was higher with increasing length of the splitter blades [6].

## 2.2 The vortex rope

At part load, pressure oscillations also originate from the vortex rope in the draft tube [8]. The purpose of the draft tube is to reduce the exit velocity of the flow in order to minimize loss of kinetic energy and recover energy at the outlet. The flow leaving the runner under optimal conditions has nearly no rotational velocity component and is virtually axial. During part load or high load operation, the exiting flow contains a swirl component that generates a vortex at the centre of the flow downstream of the runner. Excessive swirl leads to instabilities that introduce pressure fluctuations and eventually the draft tube surge. A helical vortex, the vortex rope, is characteristic of the draft tube surge. This flow is self-excited unsteady because the flow within the draft tube varies with time, while the discharge from the draft tube may or may not vary with time [17]. The vortex rope can cause serious problems for hydraulic equipment as powerful flow pulsations lead to strong vibrations of the turbine structure. Resonance can even lead to turbine structural failure [9]. The draft tube vortex frequency, or Rheingans frequency [2], is given by

$$f_R \cong \frac{f_n}{3.6} \quad [Hz] \tag{2.11}$$

Simulation of the vortex rope is very time consuming. It takes considerable time for the frequency of the vortex rotation to stabilize and for the vortex to assume its final shape. According to Jošt and Lipej, as much as 40 runner revolutions is usually necessary in order to get stable values for pressure pulsation frequency and amplitudes [7]. Yexiang et al. ran simulations for 3600 time steps in order to capture the vortex rope [10].

## 2.3 Vortex shedding

For almost any bluff body, vortex shedding starts at approximately Re>35, and persists over a wide range of Reynolds numbers. Vortex shedding is the separation that occurs in the wake of the body, with pairs of vortices alternately shed from the upper and lower part of the rear surface. The wake becomes more turbulent and complex with increasing Reynolds numbers, but can still be detected at Re=107 [18]. Vortex shedding can cause fatigue failure of the stay vanes in Kaplan turbines. It can also cause noise from the trailing edges of the runner blades in Francis turbines, indicating that the trailing edges need modification [19].

## 2.4 Other fluctuations

Some pressure fluctuations can arise from inequalities in the system, for example if a steady flow of water is interrupted by a sudden closing of the main valve, or even a change in the guide vane position. These fluctuations are independent of the rotational speed of the turbine, but depend on the geometry of the waterway and the propagation speed of the pressure wave, i.e. the speed of sound in water. These pressure fluctuations are due to the elasticity of the water and are known as the water hammer [20].

## 2.5 Operating regimes

This section briefly describes the different flow regimes associated with different loads.

**High load** Fluid in the runner tends to flow towards the machine axis, creating a swirl against the runner rotation in the draft tube. Because of a low static pressure in the swirl center, cavitation is often generated in the vortex core. Periodic pressure fluctuations due to rotor-stator interaction is dominant at high load and around BEP in the vaneless space for high head Francis units [5].

**Best Efficiency Point (BEP)** The inflow to the runner blades coincides with the blade angle, and draft tube flow is stable with a low swirl intesity [5].

**Part load** The fluid in the runner flows outwards to the outer region of the machine. The flow leaves the runner with a swirl rotating in the direction of the runner. This outflow leads to backflow in the center of the draft tube cone and a vortex rope of helical shape. Furthermore, the inflow on the runner is not consistent with the blade angle which can cause secondary flow effects [5].

**Speed No Load (SNL)** The flow patterns of part load is even more accentuated. The backflow region of the draft tube extends into the runner. Cavitating channel vortices are produced in the runner which leads to high amplitude, stochastic pressure fluctuations. SNL is not considered in this thesis.

## 2.6 About the turbine

The model turbine at the Waterpower Laboratory at NTNU is a Francis type turbine. It includes a spiral casing, a distributor with 14 stay vanes integrated into the spiral casing and 28 guide vanes. The runner has 15 blades with an additional 15 splitter blades. The draft tube is an elbow-type. The test rig is a hydraulic system capable of generating $\approx 16m$ head for open loop, and $\approx 100m$ head for closed loop [16].

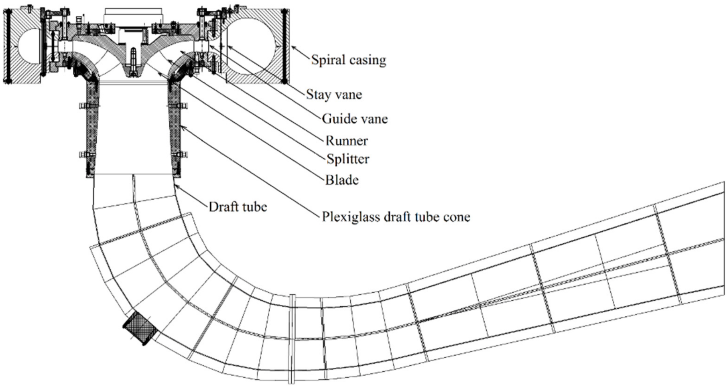

*Figure 2.1: 2D view of the turbine model. Retrieved from [16]*

## 2.7 Turbulence modelling

Flow in a hydraulic turbine is swirling and very turbulent. Because of very small turbulence scales, like the Kolmogorov microscales, it is very time-consuming and computational heavy to solve all scales because it would require a very fine computational mesh. In order to cut computational time, turbulence modelling is therefore necessary. The choice of turbulence model is important because the calculated results will differ depending on the model chosen [7] [21]. According to a study by Magnoli and Schiller, turbulence modelling is crucial for a proper turbine flow simulation [8].

Which turbulence model to apply relies on the subject at hand. According to Thapa et al., the Shear stress model (SST), realizable k-$\epsilon$ model and standard k-$\epsilon$ model is sufficient when analysing RSI and pressure pulsations. If the vortex rope is to be predicted, turbulence models such as RNG k-$\epsilon$, SAS-SST or LES will give more accurate results. But these will in turn require a finer grid and larger computational effort and thereby simulations take longer time [4].

## 2.8 Hill diagrams

It is convenient to use a hill diagram in order to get an overview of how a turbine performs under different operating conditions. Hill diagrams are based on dimensionless parameters. The dimensionless volume flow $Q_{ed}$ is plotted against dimensionless rotational speed $n_{ed}$ [14]. These are given as

$$n_{ed} = \frac{nD_2}{\sqrt{gH}} \tag{2.12}$$

$$Q_{ed} = \frac{Q}{D_2^2\sqrt{gH}} \tag{2.13}$$

where $Q$ is the volumetric flow through the turbine, $D_2$ is the outlet diameter, $n$ is the rotational speed and $H$ is the effective head.

Creating a hill diagram in the laboratory consists of measuring the flow, head and torque. The guide vane opening is kept constant while the rotational speed is varied. The procedure is then repeated for several other guide vane openings.

# 3 Method

Much of the content in this chapter have been reproduced with some alterations from the authors's project thesis [3].

## 3.1 Computational domain

Because the flow in the different turbine components are connected and interact with one another, individual component analysis does not correspond correctly to experimental data. A full analysis on the turbine with spiral casing, distributor, runner and draft tube is necessary for a complete simulation of the flow through the turbine [8]. This is very time consuming. A simulation of the entire water way was not feasible. The focus of this master thesis is on the interaction between the guide vanes and runner. The computational domain was therefore limited to guide vanes, runner and part of the draft tube. The draft tube is large and thereby it requires a lot of cells. Reducing the draft tube into only a small section saves a lot of computational time by reducing the number of cells substantially. The guide vanes and runner strongly influence one another because of dynamic forces, and as the pressure pulsations from RSI's are very prominent in high head units, this focus is acceptable. Seidel et al. showed that the gate passing frequency was the dominating frequency for a high head Francis unit, and that fatigue life therefore was governed nearly exclusively by RSIs [13] [4]. The entire computational domain can be seen from figure 3.1. It was also assumed that no leakage occurs.

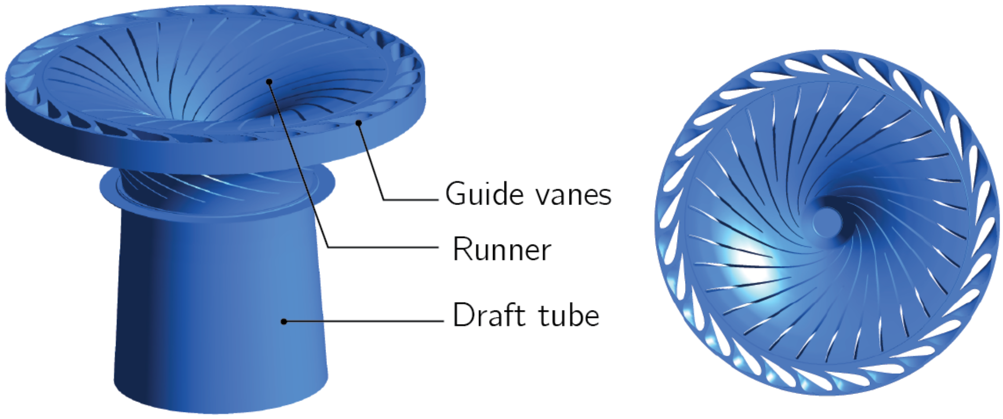

*Figure 3.1: An overview of the modelled flow passage.*

## 3.2 Software and hardware

The CFD simulations were carried out with ANSYS CFX version 18.1. Steady state simulations were run on an Intel Xeon E5-1650 processor with six cores and 64 GB RAM. Transient simulations were run on the cluster Fram [22].

## 3.3 Mesh

The mesh for the runner and the draft tube cone was provided by EDR Medeso. The guide vane geometry complete with blocking and mesh was provided by Chirag Trivedi. The meshes for the runner and the guide vanes were made separately for different studies connected to Francis-99 [23]. Both the geometry and blocking for the guide vanes therefore had to be modified in order for the guide vane mesh to fit together with the runner mesh. The outlet from the guide vanes was therefore elongated by approximately 1.5 mm, and the channel height adjusted with 0.4 mm on both hub and shroud side using ICEM. A grid convergence study was considered unnecessary because the meshes had previously been tested for convergence and had been used in previous studies.

Because simulations were going to be executed for several different guide vane openings it was necessary to find a method for changing the guide vane angle. Two options were considered for achieving this: Using mesh deformation in CFX, or actually rotating the guide vane geometry and create a mesh for each value of $\alpha$. Jakobsen and Aasved Holst simulated transient load changes using mesh deformation in CFX [24]. Their results agreed well with experiments, but the mesh elements close to the guide vanes were skewed after the deformation as can be seen from figure 3.2.

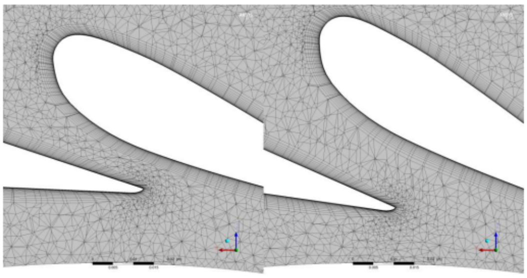

*Figure 3.2: Figure shows the final guide vane position during part load (left) and high load (right) when using mesh deformation. Retrieved from [24].*

While mesh transformation is suitable when considering a transient load change, for simulations with a fixed guide vane position it was decided to rotate the guide vanes in order to preserve a high quality mesh and maintain complete control over the mesh. A total of eleven different guide vane meshes were made, ranging from $\alpha = 4°$ to $\alpha = 14°$. The lowest pre-mesh quality was 0.27 for $\alpha = 4°$. Rotation in ICEM was achieved by rotating the geometry and then rotating and updating the blocking for a single guide vane. The mesh was then generated for further use in CFX. Because the mesh was set up as periodic it was ensured that the nodes would match up while also forcing the nodes to be rotationally periodic with one another [25]. This allowed for a single guide vane to be copied and rotated around the rotation axis in CFX without needing to specify interfaces in between each guide vane.

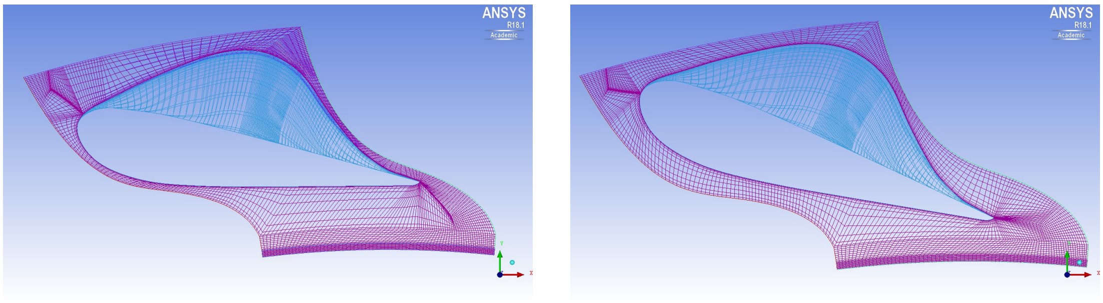

*(a) Mesh for $\alpha = 4°$.*

*(b) Mesh for $\alpha = 14°$.*

*Figure 3.3: Comparison of meshes for two different alphas.*

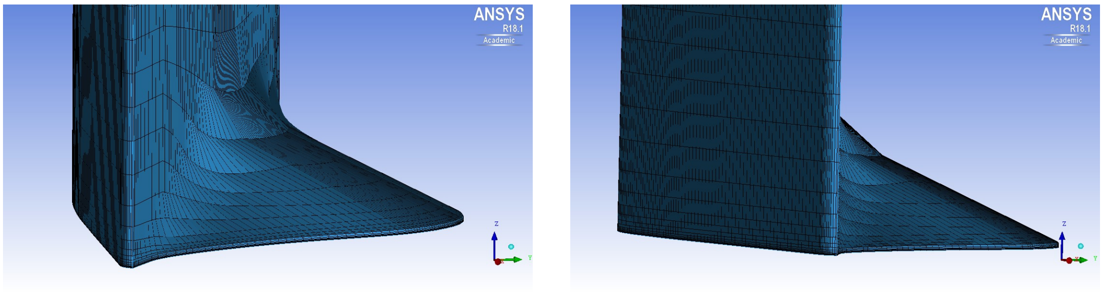

*(a) Mesh for $\alpha = 10°$.*

*(b) Mesh for $\alpha = 10°$.*

*Figure 3.4: Figure shows the fillet on the shroud side of the guide vane. It can be seen that the curvature is not completely smooth. This could be solved by adding more cells, but this would in return require longer simulation running time.*

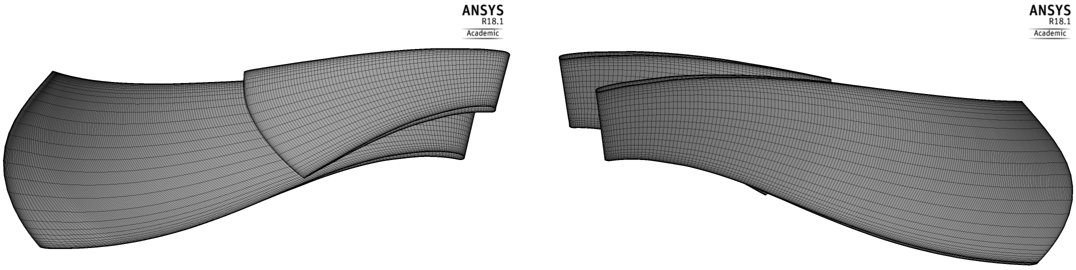

*(a) Runner mesh pressure side.*

*(b) Runner mesh suction side.*

*Figure 3.5: Figure shows the mesh for a main blade and a splitter blade.*

| Domain | Number of Elements |
|---|---|
| Guide vanes | 7948080 |
| Runner | 9220050 |
| Draft tube | 4494400 |
| Total | 21662530 |

*Table 3.1: Mesh statistics. The number of elements in total and for each domain.*

## 3.4 Turbulence model

The Shear Stress Transport (SST) model was used for all the simulations because it can provide a good estimate both close to walls and in the free stream. The SST turbulence model is an industry standard and uses the k-$\omega$ model close to the wall, but because that model is sensitive to the inlet free stream turbulence properties, it utilises the k-$\epsilon$ model in the free stream. SST is merited for good performance in adverse pressure gradients and separating flow [4] [26]. The SST model is expressed mathematically as

$$\frac{D\rho k}{Dt} = \tau_{ij}\frac{\partial u_i}{\partial x_j} - \beta * \rho\omega k + \frac{\partial}{\partial x_j}\left[(\mu + \sigma_k\mu_t)\frac{\partial k}{\partial x_j}\right] \tag{3.1}$$

$$\frac{D\rho\omega}{Dt} = \frac{\gamma}{\nu_t}\tau_{ij}\frac{\partial u_i}{\partial x_j} - \beta\rho\omega^2 + \frac{\partial}{\partial x_j}\left[(\mu + \sigma_\omega\mu_t)\frac{\partial \omega}{\partial x_j}\right] + 2(1 - F_1)\rho\sigma_{\omega 2}\frac{1}{\omega}\frac{\partial k}{\partial x_j}\frac{\partial \omega}{\partial x_j} \tag{3.2}$$

## 3.5 Simulation setup

All simulations were performed at $n_{ed} = 0.18$. It should be noted that the rotational speed, $n$, varied for the experimental measurements due to fluctuations in the waterway. In order to get results as close to the experiments as possible, the simulations were run at the measured $n$ which varied between $n = 333.5$ rpm and $n = 340.0$ rpm.

The entire fluid domain was formed in CFX by combining the components with a GGI (General Grid Interface) between the guide vanes and runner, and a GGI interface between runner and draft tube. GGI permits a connection where the connected surfaces does not match whether it is a non-match of node location, element type, surface extent, surface shape or even non-matching of the flow physics across the connection [27]. A rotating domain was set up for the runner in CFX Pre, while stationary domains were set up for guide vanes and draft tube. Frozen Rotor model was chosen as the connection between the rotating and stationary domains for the steady state simulations. Using Frozen Rotor approach, the frame of reference is changed, but the relative components across the surface is fixed. It produces a steady state-solution with some account of the interaction between the two frames of reference. This approach is the least computational heavy of the three models to choose from in ANSYS. However, transient effects are not captured with Frozen Rotor, meaning that for transient simulations another connection type had to be used. The Transient Rotor-Stator option was used for transient simulations because it can predict the transient interaction between a stator and a rotor passage as it accounts for all interaction effects between components that are moving relative to one another. The downside is that this model is computational heavy and require a lot of disk space [28].

Monitor points were set up in CFX at the location of the pressure sensors in the actual model turbine. Several more points were set up in CFX than was actually used in the experimental measurements, meaning that only some of the monitor points were used for further analysis. The points used for further analysis in this thesis are depicted in figure 3.6.

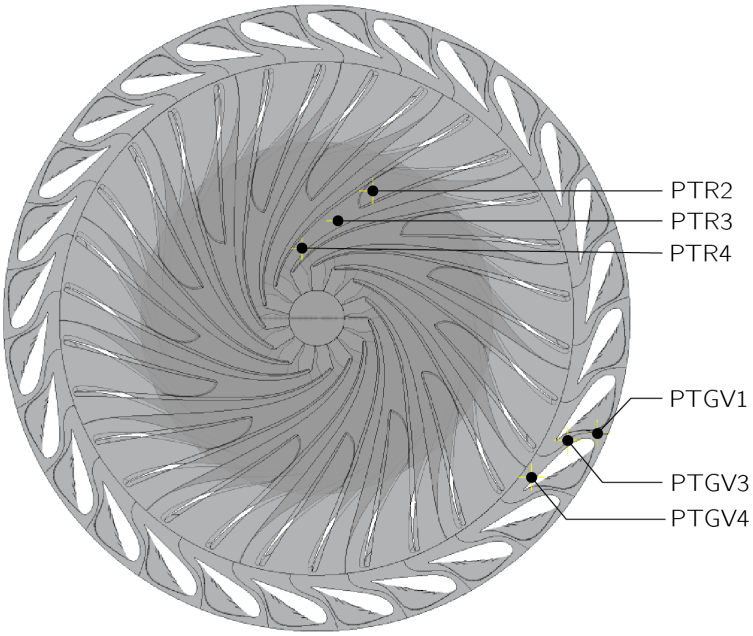

*Figure 3.6: An overview of the location of the monitor points used for simulations and analysis.*

### 3.5.1 Boundary conditions and initial values

In addition to choosing a turbulence model, in order to achieve results that are close enough to experimental values, reasonable boundary conditions have to be determined [11].

**Inlet** Volumetric flow is used as inlet condition. The flow direction is angled as if the water was leaving the stay vanes. This is achieved 360° around the turbine by using cylindrical coordinates. Values from experimental measurements were used for the volumetric flow.

**Outlet** The mean pressure at the outlet of the draft tube cone is unknown. There are in fact pressure sensors at that location, but these measure the change in pressure. Hence the mean pressure of these measurements are zero. Therefore the relative pressure was set to 0 Pa at the outlet. CFX will adjust the pressure at the inlet to meet this boundary condition and therefore yield negative pressure for parts of the turbine. That is of course physically impossible, but because the interest of this thesis is pressure pulsations, this is a reasonable assumption. The pressure term in the Navier-Stokes equation is for pressure change, which should be correct.

**Walls** No slip condition is applied at solid walls. This means that $u = v = w = 0$ along solid walls where $u$, $v$ and $w$ are the velocity components in the three directions of the coordinate system. No slip is also applied at runner blades and guide vanes.

**Initial values** Steady state results were used as initial values.

**Timestep** In their numerical analysis of RSI's, KC et al. used a time step that corresponded to a 2° rotation of runner [4]. That runner had 13 blades, which means that they would have approximately 14 points between each time a runner blade passes a guide vane. For the case of the runner in the Waterpower Laboratory, with 15 main blades and 15 splitter blades, a 2° rotation of runner would correspond to only 6 points between each time a blade is passing a guide vane. With only 6 points, there would be little information to retrieve the fundamental frequency from. Previous simulations have shown that a time step $\leq 1°$ can give reasonable agreement with experimental results [29]. A time step corresponding to a rotation of 0.96° was chosen for the simulations, giving 375 points for one revolution and thereby 12.5 points between each blade passing. The simulation was then set to run for five runner revolutions. According to a previous study of the same turbine, the flow at the outlet of the complete draft tube was observed to be periodically uniform after two revolutions of the runner with a time step of 0.5° [12]. Only the two last runner revolutions were used for further analyses in MATLAB as these were sufficiently periodic.

## 3.6 Steady state analysis

The first step in order to get the transient results was to get a steady state solution. This results file was used as initial values for the transient simulations. All simulations were performed at $n_{ed} = 0.18$. Values from experimental measurements were used for both the runner rotation and the volumetric flow rate.

The convergence criteria for the steady state simulations was set to $RMS < 10^{-4}$. Simulations were set to run for 1000 iterations if the convergence criteria was not met.

## 3.7 Transient simulations

After about two revolutions the pressure pulsations were quite stable. To ensure periodicity the transient simulations were carried out for 1875 time steps, corresponding to five runner revolutions. The two last revolutions were used for further analysis in MATLAB.

## 3.8 Frequency analysis in MATLAB

Both the steady state results and the transient results were analysed using MATLAB. A simple comparison between torque and efficiency was made for the steady state results to make sure the results were acceptable for further use in transient analysis.

In order to identify the different frequencies from the transient simulations, the data has to be processed. The Fourier Transform transforms a periodic signal from the time domain to the frequency domain. It is a way to decompose an otherwise erratic signal into their constituent frequencies [30]. The Discrete Fourier Transform (DFT) is used when working with discrete data. It is defined as

$$y_m = \sum_{k=0}^{N-1} x_k e^{-2\pi i \frac{mk}{N}} \qquad m = 0, ..., N-1 \tag{3.3}$$

The DFT takes a vector of N complex numbers $x_k$, k=0,...,N-1, and transforms it into a vector of N complex numbers $y_m$, m=0,...,N-1. The practical implementation of DFT on a computer, however, is often the Fast Fourier Transform (FFT) algorithm [31].

The frequency spectra is important to identify amplitudes and relevant frequencies. The pressure data was transformed from the time domain to the frequency domain using a Fast Fourier Transform (FFT). FFT assumes a periodic signal with period N and infinite duration. Of course, in practice the signal is finite and we get some discontinuities because of windowing that results in spectral leakage in the frequency domain. Because windowing results in the sinc-function which has side lobes in the frequency domain, there will be an increase in the bins around the relevant frequencies as a result of spectral leakage from the main lobe.

$$sinc(x) = \frac{sin(x)}{x} \tag{3.4}$$

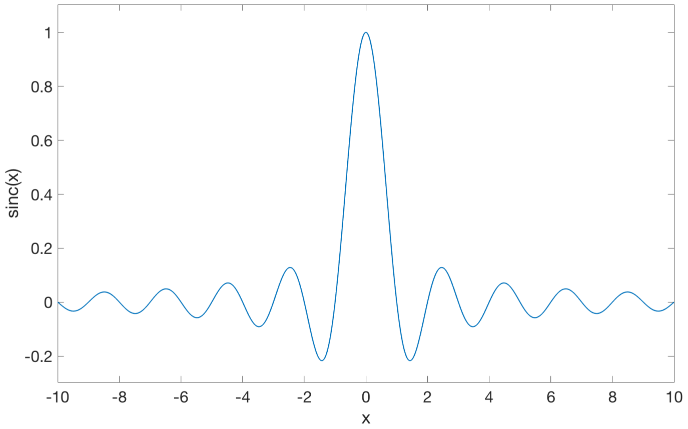

*Figure 3.7: Representation of the sinc(x) function and the resulting side lobes.*

Obtaining the frequency spectrum was achieved by first removing linear trends using `detrend` in MATLAB, then using the `fft`-function on the simulation data. Welch's method, the function called `pwelch` in MATLAB, was used on the measured pressure data. Welch's method is used to estimate spectral density and can reduce the effect of spectral leakage. The method is suitable for imperfect and finite data because it reduces noise, but in exchange it reduces the frequency resolution. The data is divided into segments, then a window function is applied to each segment. Overlapping the segments will then reduce variance and give better results [31]. Welch's method was also tested on the numerical results, but as the frequency spectrum was identical with both regular FFT and Welch, it was decided to use regular FFT. Regular FFT was also tested on the experimental results, but this introduced more spectral leakage.

It should also be noted that highpass filters were applied to remove low frequencies that were not of interest. These filters were generated using filterBuilder in MATLAB. The amplitudes and frequency spectra for the simulations were then compared to the experimental measurements.

(PAGE INTENTIONALLY LEFT BLANK)

# 4 | Results and discussion

This section provides the results obtained through simulations and compares them to experimental measurements.

## 4.1 Steady state results

To verify that the steady state results were reliable, the torque and efficiency was compared to experimental measurements. Torque was estimated in CFX using the built in function `torque_z()@location` in CFX Post that calculates the torque in the z-direction at the specified location. In this case the torque was estimated by summation of the torque on the blades, hub and shroud. Note that the torque on the hub and shroud has the opposite direction of the torque on the blades. Efficiency is calculated from

$$\eta = \frac{\tau\omega}{gH\rho Q} \tag{4.1}$$

where $\tau$ is the estimated torque, $\omega$ the angular velocity, $g$ the gravity constant, $H$ is the head, $\rho$ the density and $Q$ the volumetric flow. All of these parameters were estimated using CFX post. At $\alpha = 10°$ we have our best efficiency point for both the numerical results and the measurements.

For all simulations the convergence criteria was met, except for $\alpha = 5°$, $6°$, $7°$ and $12°$. These simulations ran for 1000 iterations without the convergence criteria being met, but it was apparent that there was little change, and that the solution was sufficient for further use in transient simulations.

Because the inlet and outlet of the simulation differed from the actual model turbine, only comparison of torque and efficiency was possible. These are listed in table 4.1 and shown in figures 4.1 and 4.2.

The smallest deviation from experimental results for torque was 1.78 percent for $\alpha = 13°$, and the biggest was 10.34 percent for $\alpha = 6°$. For the efficiency the smallest difference was 3.36 percent for $\alpha = 9$ while the biggest difference was 7.24 percent for $\alpha = 4°$. Even though these differences are quite large, it can be seen from figures 4.1 and 4.2 that the numerical results follow the same trend as the experiments. The simulations overpredict both the torque and efficiency for all guide vane openings, with the exception of torque at $\alpha = 12°$. Zhao Yaping et. al did a performance study for the same model turbine as in this thesis where they compared the SST turbulence model to the standard k-$\epsilon$ turbulence model. The study showed that a larger circulation deviation of the SST turbulence model lead to a higher hydraulic efficiency than when using standard k-$\epsilon$. The difference between the experimental and numerical values for efficiency and torque when using standard k-$\epsilon$ was smaller than when using SST [11]. Smaller difference in efficiency was also documented by Trivedi when doing simulations for the same turbine when comparing k-$\epsilon$ and SST [12]. Magnoli and Schilling also achieved best results with the k-$\epsilon$ turbulence model for their steady state solution [8]. Hence, for better accuracy in torque and efficiency one could try using standard k-$\epsilon$ turbulence model. Zhao Yaping et. al also suggested that a reason for the torque calculation inaccuracy in the numerical simulations was a result of unstable flow, such as impact, flow separation and vortex. And that this would lead to a numerical efficiency that was greater than that for the experimental data [11].

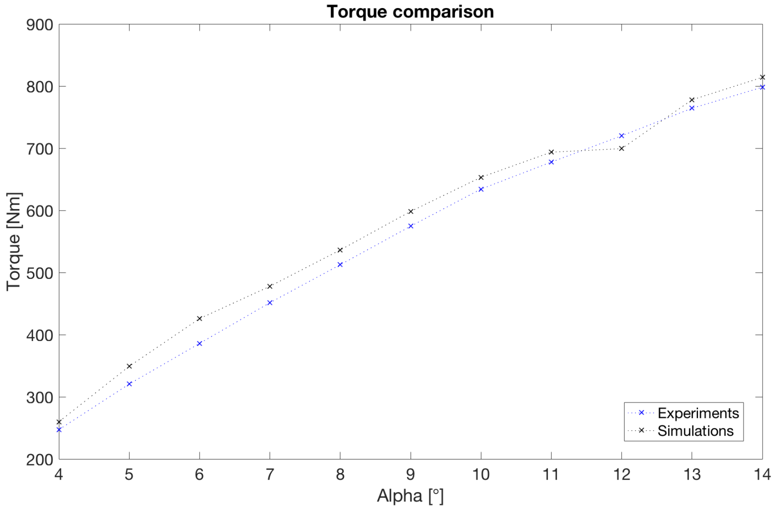

*Figure 4.1: Comparison of torque between experiments and numerical results.*

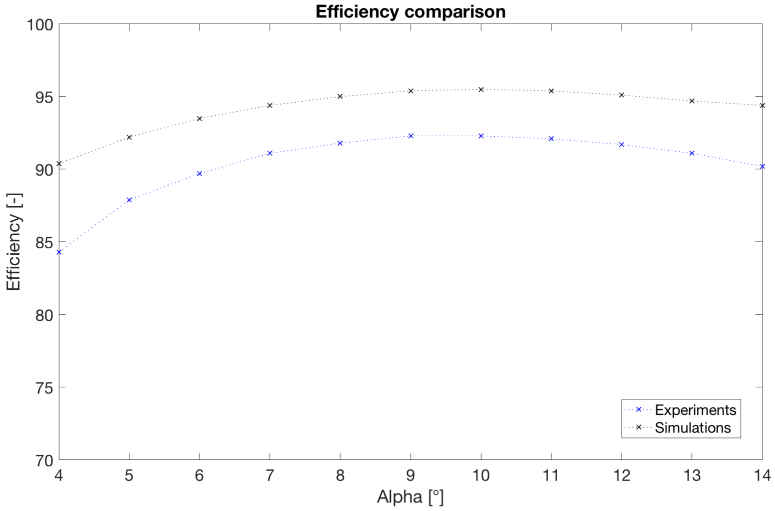

*Figure 4.2: Comparison of efficiency between experiments and numerical results.*

The torque is underpredicted at $\alpha = 12°$ as one can see from figure 4.1. An early theory was that the mesh for $\alpha = 11°$ was accidentally used instead of the mesh for $\alpha = 12°$

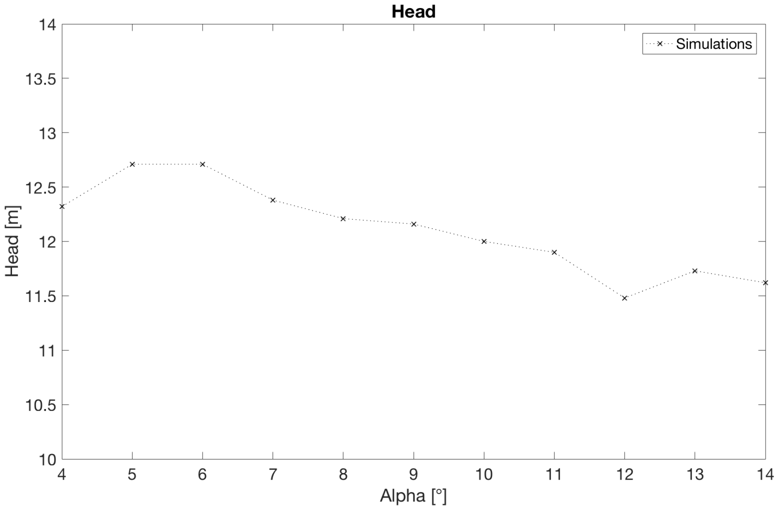

*Figure 4.3: The predicted head for the simulations.*

because of the similarity in torque with $\alpha = 11°$. However, the meshes and boundary conditions were double checked and the simulation run a second time, still giving the same underpredicted torque. It is also evident from the figures that the efficiency is correctly calculated. This might indicate that the head is being underpredicted as well because efficiency is proportional to $\frac{\tau}{H}$ as seen from equation 4.1. Hence, an underpredicted head and an underpredicted torque will yield correct efficiency because of the the definition of $\eta$ in equation 4.1. Because of different definitions of head in the simulations and experiments (i.e. the inlet and outlet are defined at different locations), head is not comparable. In order to check whether the head was in fact underpredicted, the relation between the head at different alphas were examined for simulations only as seen from figure 4.3. The head follows a consistent trend, but suddenly drops at $\alpha = 12°$, confirming that the head is underpredicted by the steady state simulation as well.

Errors may be systematic, or may be associated with random fluctuations which tend to have a Gaussian distribution if the errors are truly random. In CFD, the random errors can only be introduced by the user, e.g. by setting a value incorrectly. However, all values and meshes were double checked, but the same error in torque and head occurred. Thus it is assumed that this could be a systematic error related to numerical uncertainty. Because one is representing a continuous system by a finite length and discrete approximation, error becomes inherent to the process. According to Freitas, it is understood that systematic errors are created by those terms truncated in the Taylor series representation of derivatives [32] [33], or introduced by the iterative solution process. The error encountered at $\alpha = 12°$, if not introduced by human error, can therefore be studied through inter-comparisons based on variation of parameters, such as varying the grid resolution, variation in numerical schemes, and variation in models and model inputs [33]. However, for the purpose of this master thesis the solution was regarded as sufficient for further use in transient simulations, and going further into the error of this particular simulation is beyond the scope of this thesis. It should also be noted that the frequency spectras in section 4.2 seem to correspond well with measurements regardless of this drop in torque and head at $\alpha = 12°$.

| | Experiments | | Simulations | |
|---|---|---|---|---|
| $\alpha[°]$ | Torque [Nm] | Efficiency [%] | Torque [Nm] | Efficiency [%] |
| 4 | 247.12 | 84.3 | 259.82 | 90.38 |
| 5 | 320.55 | 87.9 | 349.07 | 92.2 |
| 6 | 385.93 | 89.7 | 425.85 | 93.5 |
| 7 | 451.46 | 91.1 | 477.84 | 94.4 |
| 8 | 512.56 | 91.8 | 536.30 | 95.0 |
| 9 | 574.50 | 92.3 | 598.31 | 95.4 |
| 10 | 634.25 | 92.3 | 653.20 | 95.5 |
| 11 | 677.73 | 92.1 | 693.71 | 95.4 |
| 12 | 720.04 | 91.7 | 699.31 | 95.1 |
| 13 | 764.25 | 91.1 | 777.89 | 94.7 |
| 14 | 798.14 | 90.2 | 814.07 | 94.4 |

*Table 4.1: Comparison between measurements and simulations for torque and efficiency.*

## 4.2 Transient results

This section focuses on the transient results. It should be noted that for most of the transient simulations the CFX solver placed a wall at portions of the outlet to prevent fluid from flowing back in. This is not an issue if the portion is small, but it could affect the results if the portion grows large, as was the case for simulations at part load. The most severe case was for $\alpha = 4°$ where the wall was placed on 56.1 percent of the faces and 49.1 percent of the area. This could be prevented by including a larger part of the draft tube, but that would in turn require more cells and longer computational time. For torque and efficiency measurements one could model just one single passage and thereby save a lot of cells. The runner mesh consisted of 9220050 elements, meaning that one passage is only 614670 elements. This would make room for including the draft tube while keeping the cell count at a reasonable level. However, a single passage would not capture the transient effects of pressure pulsations in a satisfactory manner.

### 4.2.1 Pressure contours

Because the pressure at the outlet was unknown, a relative pressure of 0 Pa was set as outlet boundary condition. As previously noted, this would yield the non physical result of negative pressure in parts of the turbine as can be seen from the pressure contours in this section. However, the change in pressure should be correct, and it is still possible to use pressure contours for identifying high and low pressure areas. This section presents pressure contours for four different guide vane openings, namely for $\alpha = 4°$, $7°$, $10°$ and $14°$.

#### Guide vanes and runner interaction

Figure 4.4 shows a pressure contour for $\alpha = 10°$ in a stationary frame of reference. Figure 4.5 shows a closer view of figure 4.4 together with contours for three other selected values of alpha. Theory suggests that the most significant pressure pulsations caused by RSI's

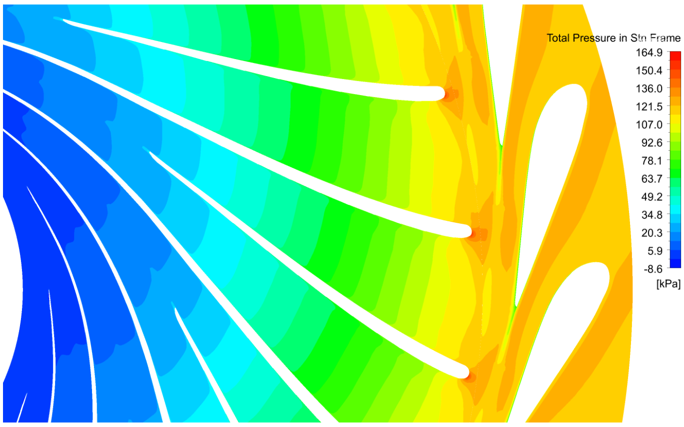

*Figure 4.4: Pressure contour for $\alpha = 10°$ in a stationary frame of reference.*

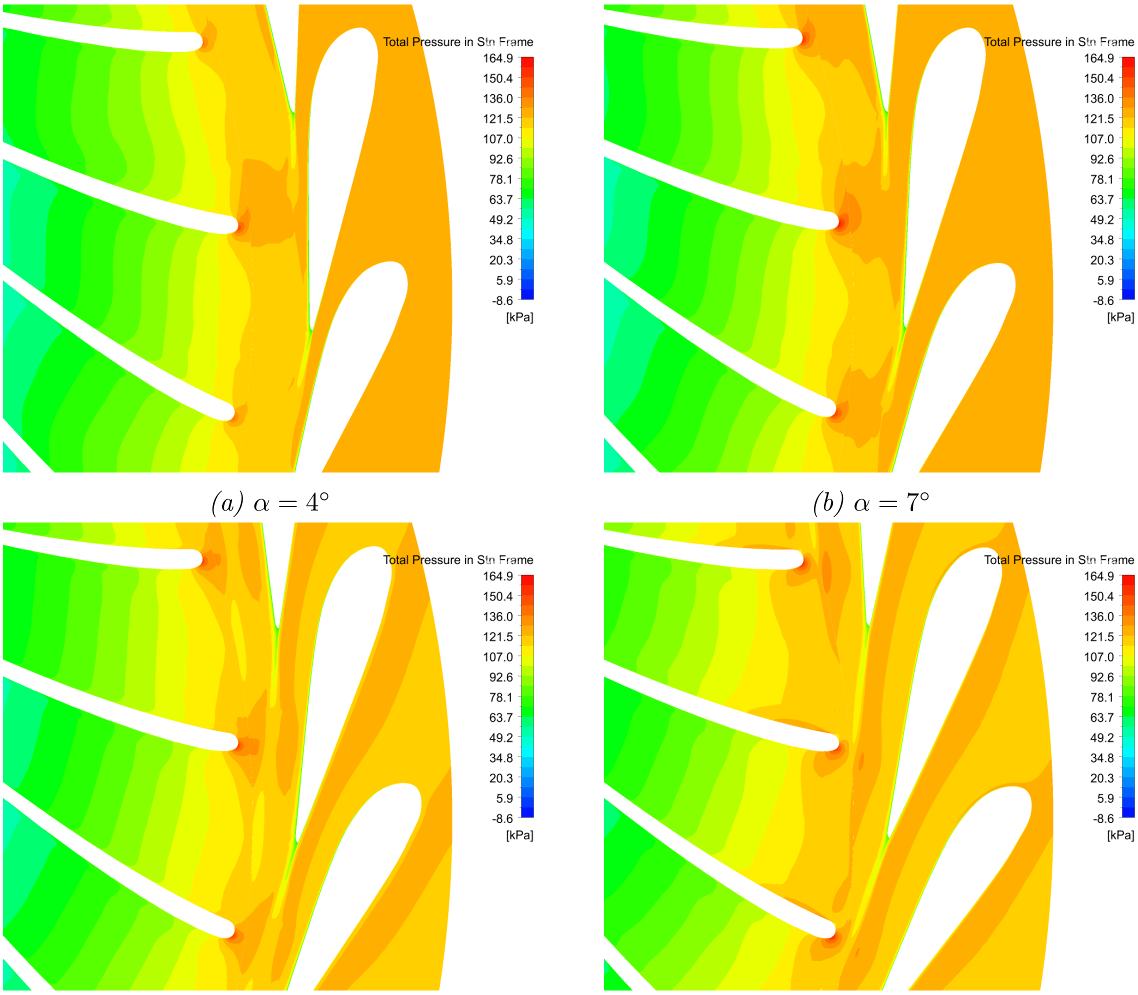

*(a) $\alpha = 4°$*

*(b) $\alpha = 7°$*

*(c) $\alpha = 10°$*

*(d) $\alpha = 14°$*

*Figure 4.5: Pressure contour for four different alphas in a statinary frame of reference.*

occur when the trailing edge of the guide vane is close to the runner. This is observable from figure 4.5. As alpha increases, the distance between the guide vane trailing edge and the runner decreases, and as a result the wake from the guide vanes are closer to the leading edge of the runner blades. Observe also that the wake grows longer for larger alphas due to the increased load.

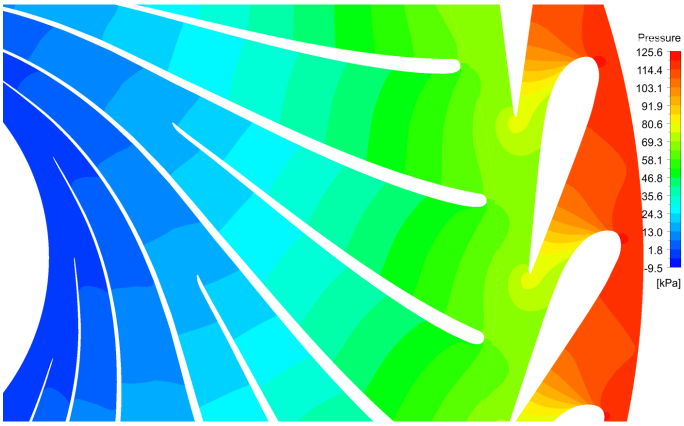

*Figure 4.6: Pressure contour for $\alpha = 10°$ in a rotating frame of reference.*

From figures 4.6 and 4.7 it can be seen that the pressure is higher further down the trailing edge of the guide vanes for $\alpha = 14°$ than for other values of alpha. This indicates that the amplitude of the pressure pulsations will be largest for full load ($\alpha = 14°$).

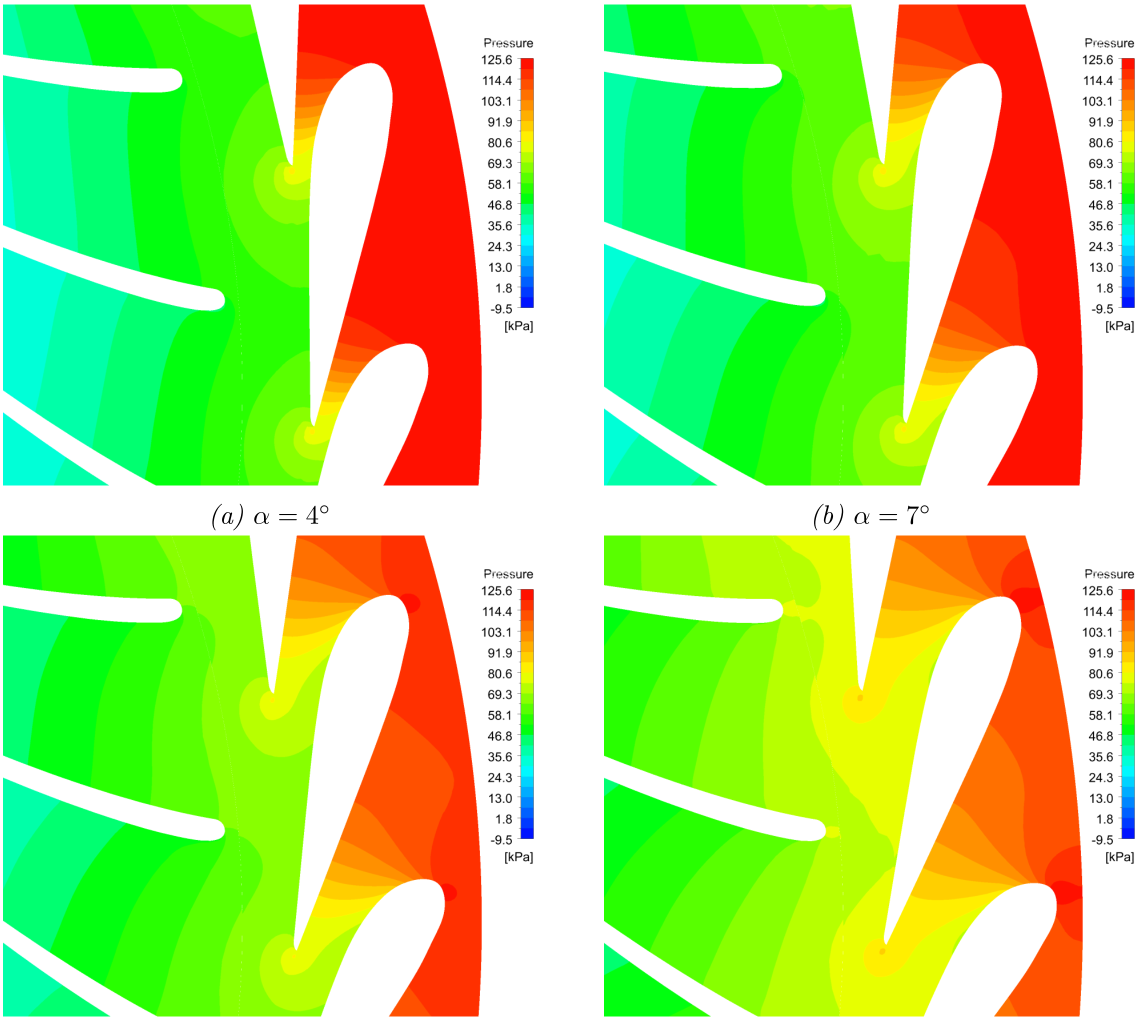

*(a)* $\alpha = 4°$ *(b)* $\alpha = 7°$

*(c)* $\alpha = 10°$ *(d)* $\alpha = 14°$

*Figure 4.7: Pressure contour for four different alphas in a rotating frame of reference.*

### Blade loading

Figures 4.8 and 4.9 shows the pressure contour for a main blade for both the pressure side and the suction side. It is clear from the figures that the pressure is the highest at the leading edge of the runner blades for $\alpha = 14°$. At $\alpha = 4°$ an asymmetric pressure distribution is observed. At part load the fluid tends to flow outwards to the outer region of the machine, and the flow leaves the runner with a large swirl component rotating in the runner rotation direction. This can lead to backflow in the center of the draft tube cone, which could explain why there was an issue at part load simulations with a wall being placed at the outlet. This backflow results in a vortex rope of helical shape [5]. The draft tube vortex frequency was not captured in the simulations because firstly, the simulations did not run long enough for the vortex rope to stabilize, and secondly, most of the draft tube was not included. At very small loads, there can be secondary flow effects between the runner blades. These cause channel vortices with low pressure regions in the vortex core [5]. These part load effects might be the reason behind the asymmetry in the blade loading, but this requires further investigation. To see how the difference in blade loading affects the solid blade, a Fluid-Structure Interaction (FSI) study must be performed.

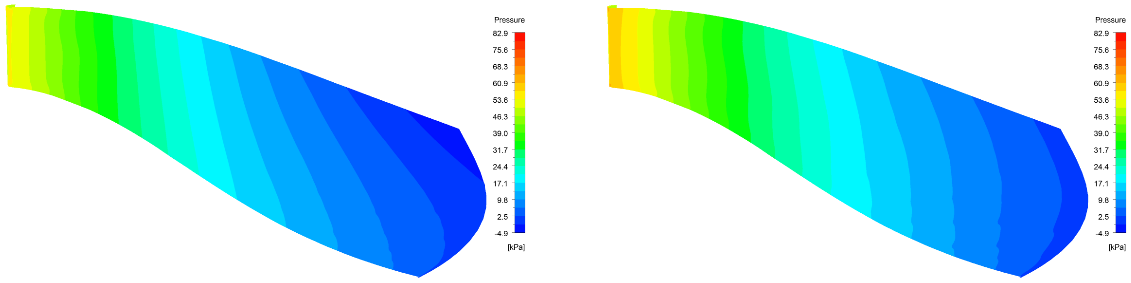

*(a)* $\alpha = 4°$ *(b)* $\alpha = 7°$

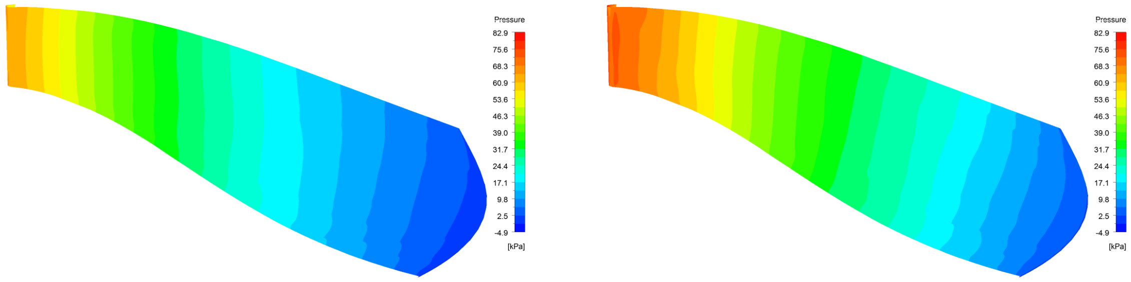

*(c)* $\alpha = 10°$ *(d)* $\alpha = 14°$

*Figure 4.8: Pressure contour for the pressure side of a single main blade.*

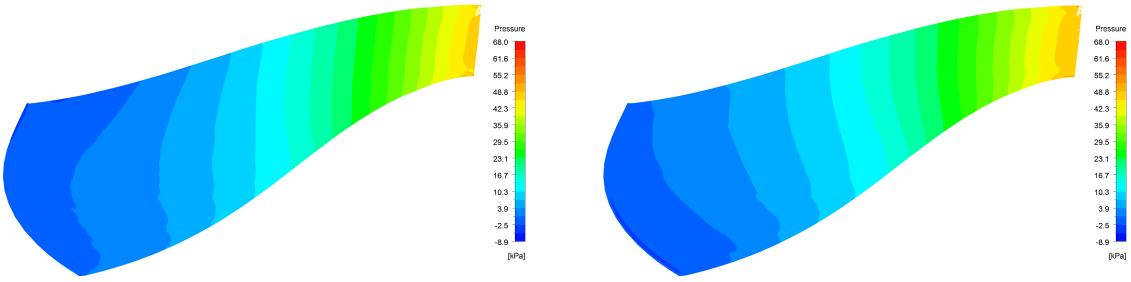

*(a)* $\alpha = 4°$ *(b)* $\alpha = 7°$

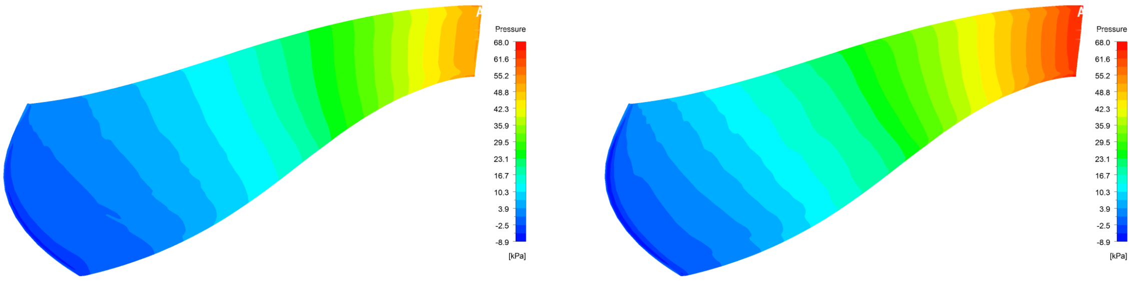

*(c)* $\alpha = 10°$ *(d)* $\alpha = 14°$

*Figure 4.9: Pressure contour for the suction side of a single main blade.*

### 4.2.2 Frequency spectrum

As noted in section 3.8, Welch's method was used on experimental data, and regular FFT on numerical data. One can see from figure 4.10 that the experimental data is characterized by noise, while the simulation data produces neat sinus curves.

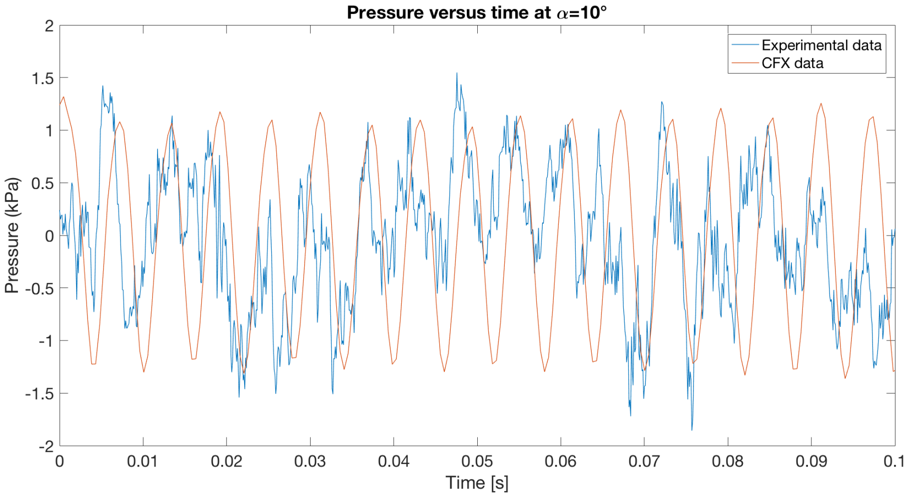

*Figure 4.10: Pressure versus time for experiments and simulations. The pressure curve for the experiments has been shifted. Because of the outlet condition, the pressure in the simulations are wrongly predicted, but change in pressure is correct.*

For the figures in this subsection, the frequency spectrums have been filtered in order to reduce noise and frequencies that are not of interest. Attenuation caused by the filters can result in a reduction in amplitude. However, it was decided to only filter out low frequencies using a highpass filter, which did not affect the amplitude of the frequencies of interest for RSI's. As previously noted, using the Welch method will give larger variance if a high frequency resolution is desired. A large variance was accepted when analyzing the experimental results in order to maintain a high frequency resolution.

The experimental measurements are of a periodic and stochastic nature and applying Welch's method will affect the amplitudes for the measurements. All amplitudes are therefore shown as relative to the highest peak, i.e. the highest amplitude always have an amplitude of 1, both for measurements and simulations for the purpose of comparing the two. All frequencies are represented as normalized against the rotational frequency of the runner, $f_n$. It should also be noted that the amplitudes of the pressure pulsations from the RSI's in the draft tube were insignificant compared to those in the runner and guide vanes, and therefore these were not included in the results.

The frequency spectrum for a sensor in the runner domain, PTR2, is depicted in figure 4.11. The figure was created using the predefined function for a Fast Fourier Transform (FFT), `fft` in MATLAB. The high peaks is the guide vane passing frequency at $28f_n$, while the smaller peaks is the second harmonic at $56f_n$.

The small spikes throughout the spectrum is spectral leakage from the FFT. This leakage is observable in all the frequency spectrums and could be reduced by running the simulations

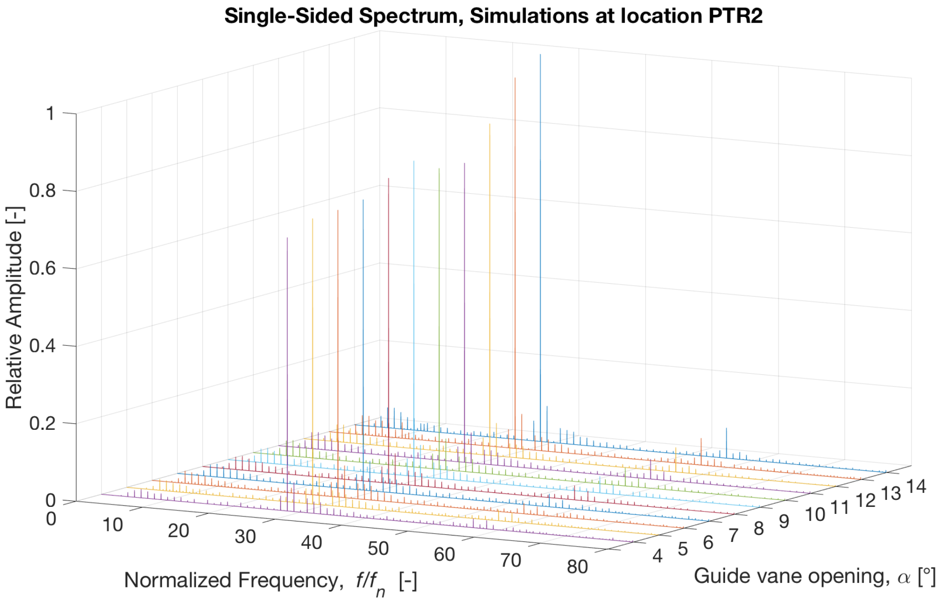

*Figure 4.11: Frequency spectrum for simulations at monitor point PTR2 at different alphas.*

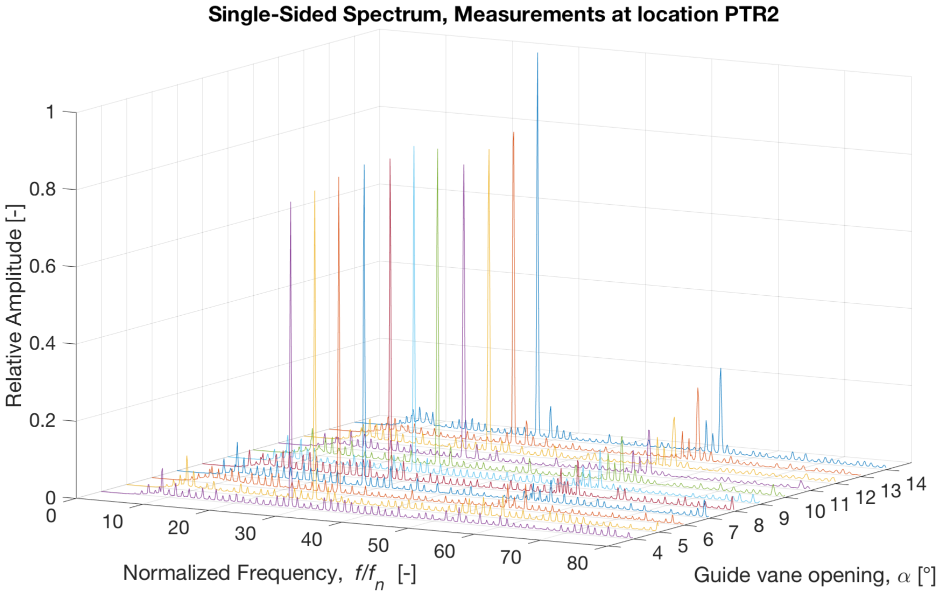

*Figure 4.12: Frequency spectrum for experimental measurements at sensor PTR2 at different alphas.*

for a longer total time, maybe as long as ten times the total time used for these simulations, in order to obtain a longer signal. However, such simulations are computational heavy and expensive. One must therefore assess how much accuracy is required. In this case the first harmonic of the guide vane passing frequency is clearly visible, but the second harmonic at part load disappears in the leakage. If the second harmonic is important then longer simulations could maybe yield better results. However, it is apparent from the figure that the first harmonic is dominant, which is consistent with Seidel [13].

The frequency spectrum of figure 4.12 was created in MATLAB using Welch's method on measurements from the master thesis "Pressure pulsation and Stresses in a Francis turbine operating at Variable Speed" [34]. The signal has been filtered with a high pass filter in order to remove prominent low frequencies that are not of interest. In the experiments the guide vane passing frequency fluctuates somewhat, but is $\approx 28f_n$. The largest deviation for the simulations from the experiments is at $\alpha = 4°$ with 1.8 percent, while the smallest is at $\alpha = 9°$ with only 0.036 percent. The high peaks are the first harmonics of the guide vane passing frequency, while the smaller peaks are the second harmonic. It is also clear from the figure that the measurements are characterized by much more noise than the simulations.

From inspection of figures 4.11 and 4.12 one can see that the simulations capture the frequency of the RSI's quite accurately. Simulations also capture the trend of the amplitudes quite well when investigating the amplitudes at a fixed location with a varying $\alpha$. The largest amplitude for the simulations and measurements at location PTR2 occurs at full load ($\alpha = 14°$), which is when the trailing edge of the guide vanes are closest to the leading edge of the runner blades. The smallest amplitude for the simulations is observed at $\alpha = 4$, while it is observed at $\alpha = 11$ for the measurements. For both simulations and measurements, the amplitudes increase from $\alpha = 4°$ until $\alpha = 9°$ where a local maximum is observed. For $\alpha = 10°$ and 11 the amplitudes decrease until the they again increase for $\alpha = 12°$, 13° and 14°. It is also seen from the figures that the second harmonic is underpredicted by the simulations. The ratio between the first and second harmonic for some alphas is listed in table 4.2. The smaller guide vane openings are not included because the amplitudes of these second harmonics were so low that they fell within the noise range.

| Alpha | Ratio simulations | Ratio experiments | Deviation (%) |
|---|---|---|---|
| 9 | 0.053 | 0.13 | -59 |
| 10 | 0.061 | 0.15 | -59 |
| 11 | 0.067 | 0.16 | -58 |
| 12 | 0.074 | 0.17 | -56 |
| 13 | 0.073 | 0.24 | -70 |
| 14 | 0.078 | 0.23 | -66 |

*Table 4.2: Comparison of the ratio between the first and second harmonic for simulations and experiments at location PTR2.*

The deviation between simulations and experiments is very large even though the simulations follow the same trend as the measurements. However, the deviation is roughly within the same range. This could indicate that there is some effect that is being captured by the experiments, but is not captured by the simulations. Much of the real dynamics in the turbine will not be reproduced in simulations, and phenomenons such as resonance and secondary flows are often lost. This could be a reason behind the large difference and should be further investigated.

When examining the ratios for the amplitudes for the second harmonic to the first harmonic for a monitor point in the guide vanes, PTGV3, the situation is different, but similar. While the second harmonic is clearly visible in the simulations (depicted in figure 4.13), it disappears in the noise range for alphas smaller than 9 for the experiments (figure 4.14). The difference in the ratios is in the same range as for PTR2, but at $\alpha = 9°$ the trend is no longer consistent as can be seen from table 4.3.

| Alpha | Ratio simulations | Ratio experiments | Deviation (%) |
|---|---|---|---|
| 9 | 0.067 | 0.072 | -6.9 |
| 10 | 0.059 | 0.15 | -61 |
| 11 | 0.066 | 0.16 | -59 |
| 12 | 0.086 | 0.17 | -49 |
| 13 | 0.086 | 0.24 | -64 |
| 14 | 0.090 | 0.23 | -61 |

*Table 4.3: Comparison of the ratio between the first and second harmonic for simulations and experiments at location PTGV3.*

What causes this deviation is unknown. It could be due to the stochastic nature of the turbine which affects the experiments, but this should be further investigated through additional experiments and simulations.

When examining the frequency spectrum for PTGV3 in figure 4.13, the simulations show a blade passing frequency of $30f_n$ which is consistent with theory. Experimental results are depicted in figure 4.14, and it is clear that also in this case the simulations reproduce the same frequencies as the experiments. The biggest deviation for the first harmonic of the blade passing frequency is 1.7 percent for $\alpha = 4°$. Observe also that the trend for the amplitudes of the first harmonic is captured quite well.

Another frequency is also quite dominating in figures 4.13 and 4.14, namely that of $15f_n$, half of the blade passing frequency. This results from the splitter blades in the turbine.

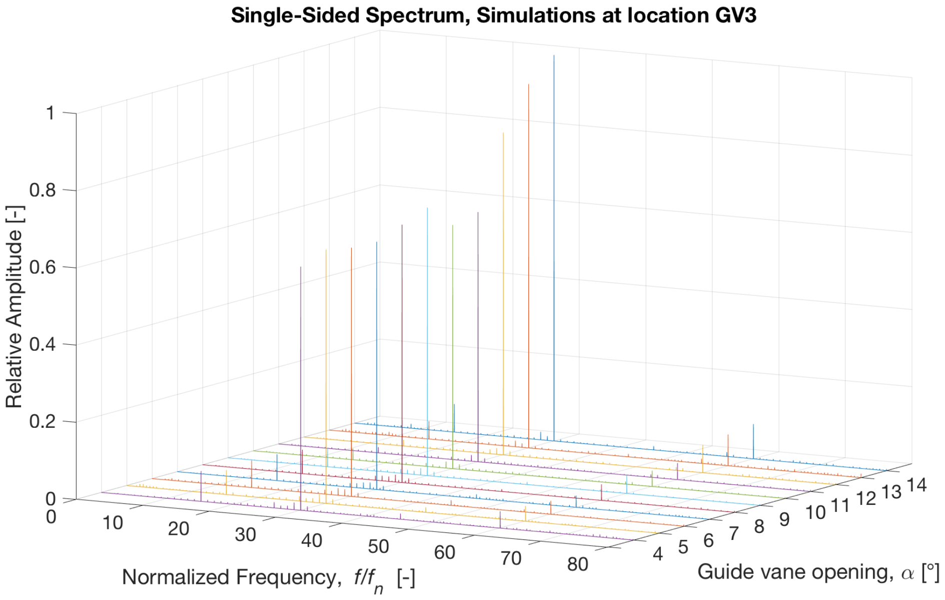

*Figure 4.13: Frequency spectrum for monitor point PTGV3 at different alphas.*

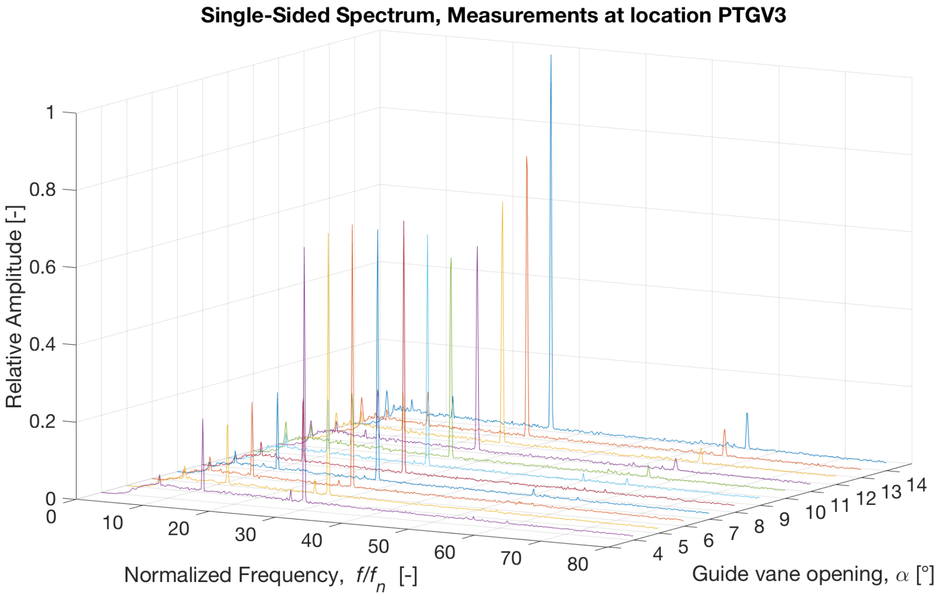

*Figure 4.14: Frequency spectrum for experimental measurements at sensor PTGV3 at different alphas.*

Predicting the frequencies of pressure pulsations through CFD is not very troublesome, but predicting the amplitudes presents a bigger challenge [5] [7]. This became more apparent when inspecting the frequency spectrums for different monitor points while keeping alpha constant.

Figures 4.17 through 4.23 show the frequency spectrum for four different guide vane openings, namely that of $\alpha = 4°$, $7°$, $10°$ and $14°$, for six different monitor points: PTR2, PTR3, PTR4, PTGV1, PTGV3 and PTGV4. There were sensors in the draft tube as well, but because the amplitudes associated with RSI's were so small compared to the amplitudes in the guide vanes and the runner, these points were not included. It can be seen from figures 4.17 through 4.22 that although the frequencies are quite accurately predicted by the simulations, the amplitudes in the guide vane domain is consistently overpredicted for the simulations compared to the amplitudes in the experimental measurements. The simulations consistently predicts the highest amplitude at PTGV4, while the measurements show that the highest amplitude occur at PTR2. This error could partly be due to mesh resolution. The mesh in the runner is coarse compared to the mesh in the guide vanes as can be seen from figure 4.15.

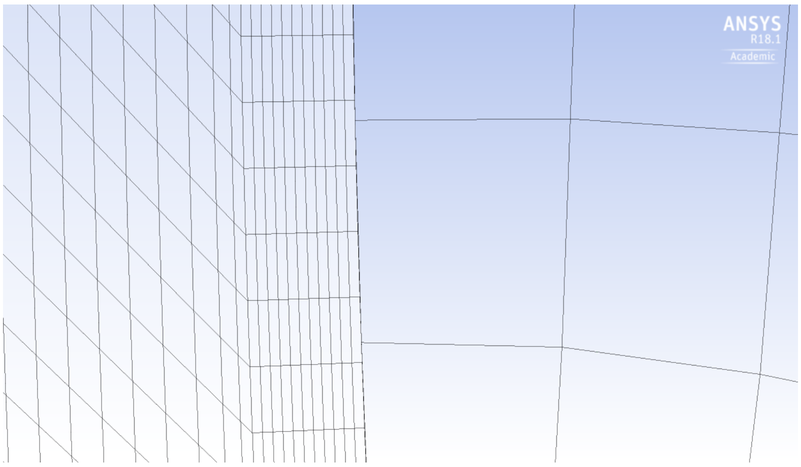

*Figure 4.15: The interface between the mesh in the guide vanes (left side) and the mesh in the runner (right side).*

The consequence is that much information is lost in the runner. While the guide vane mesh contains a lot of information in each cell, all that information is averaged when it is intercepted by the large cells of the runner mesh. According to Jošt and Lipej, a fine grid is essential when evaluating amplitudes [7], and this issue might be resolved by better agreement in mesh density between the guide vane domain and the runner domain. This is something that needs further testing. However, comparing this to previous results for the same turbine, but different simulations and experiments, it can also be seen that the amplitude in the guide vane domain is very high for the simulations compared to that of the experiments at part load. For that case, BEP did not show this same tendency [12]. While here, BEP ($\alpha = 10°$) shows very high amplitudes in the guide vanes compared to the runner. For the simulations in this thesis, it therefore seems troublesome to compare amplitudes in the runner domain to the amplitudes in the guide vane domain because of the overpredicted amplitudes in the guide vane domain. However, when investigating a specific point in either the runner or the guide vanes such as in figures 4.11 through 4.14, simulations show the same trend as the experiments.

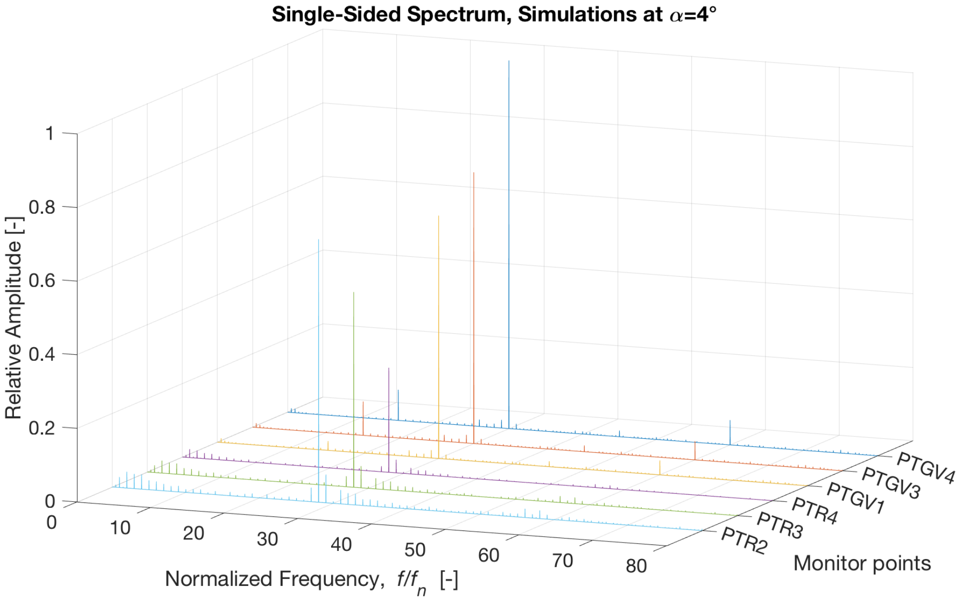

*Figure 4.16: Frequency spectrum for simulations at $\alpha = 4°$ at different monitor points.*

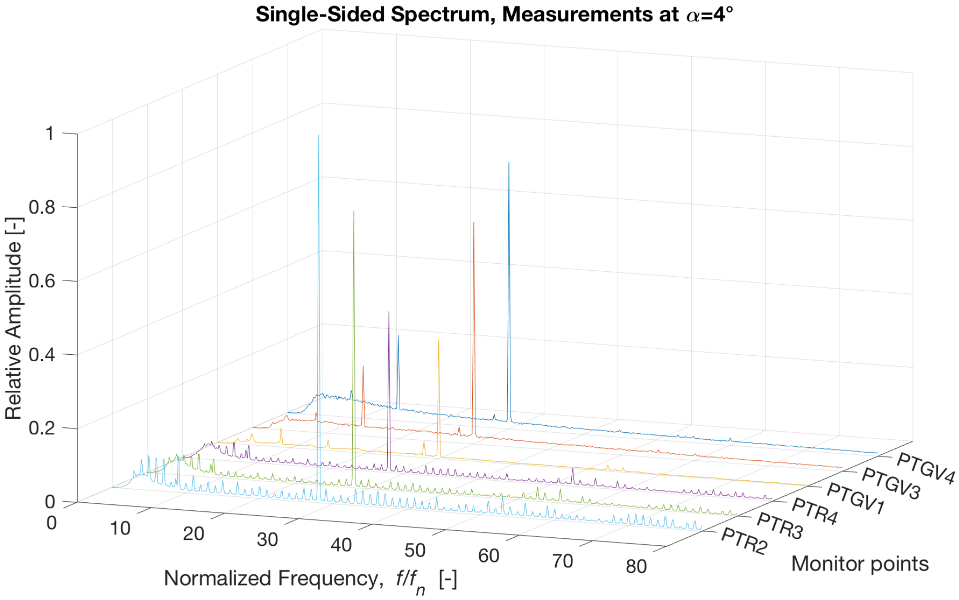

*Figure 4.17: Frequency spectrum for measurements at $\alpha = 4°$ at different monitor points.*

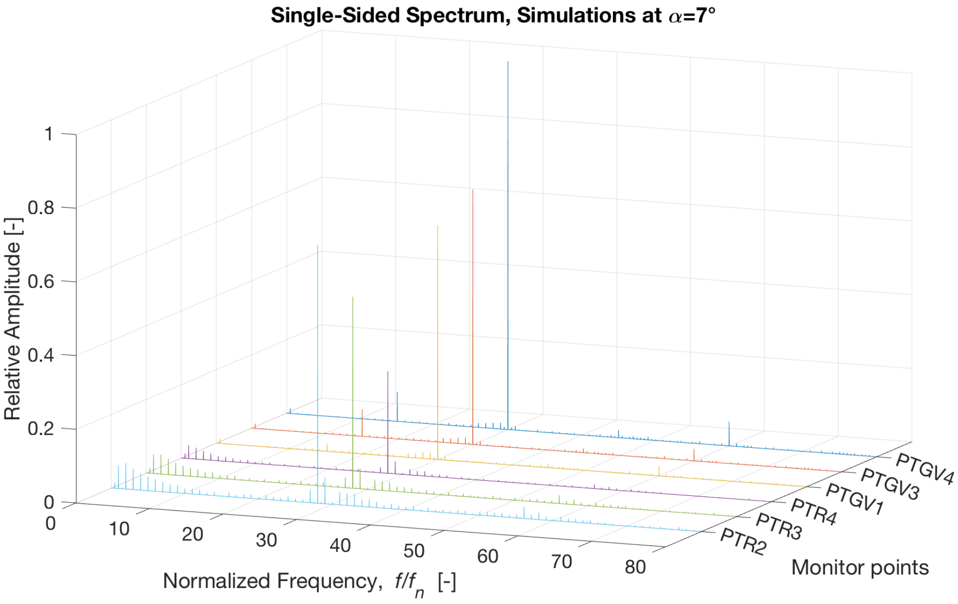

*Figure 4.18: Frequency spectrum for simulations at $\alpha = 7°$ at different monitor points.*

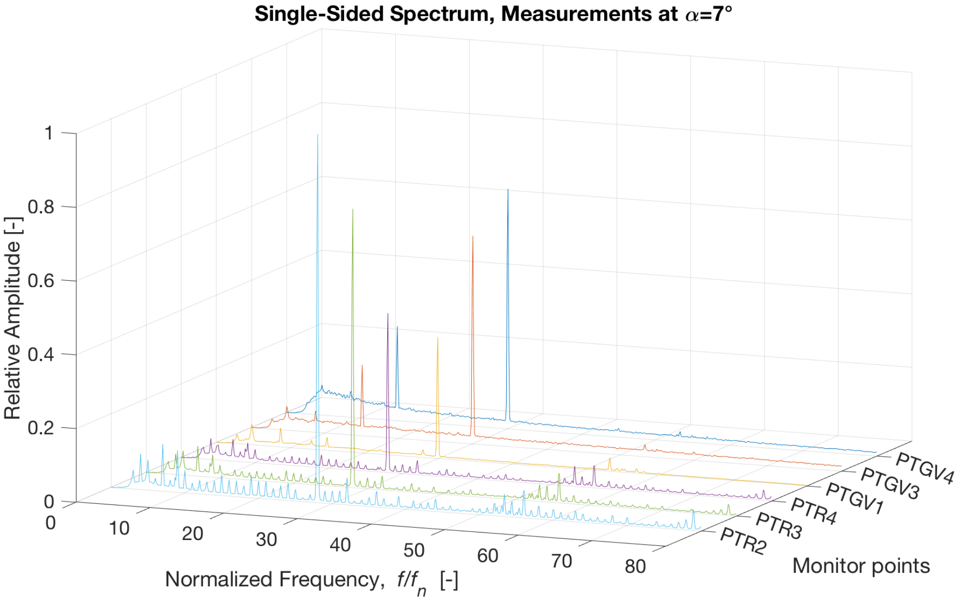

*Figure 4.19: Frequency spectrum for measurements at $\alpha = 7°$ at different monitor points.*

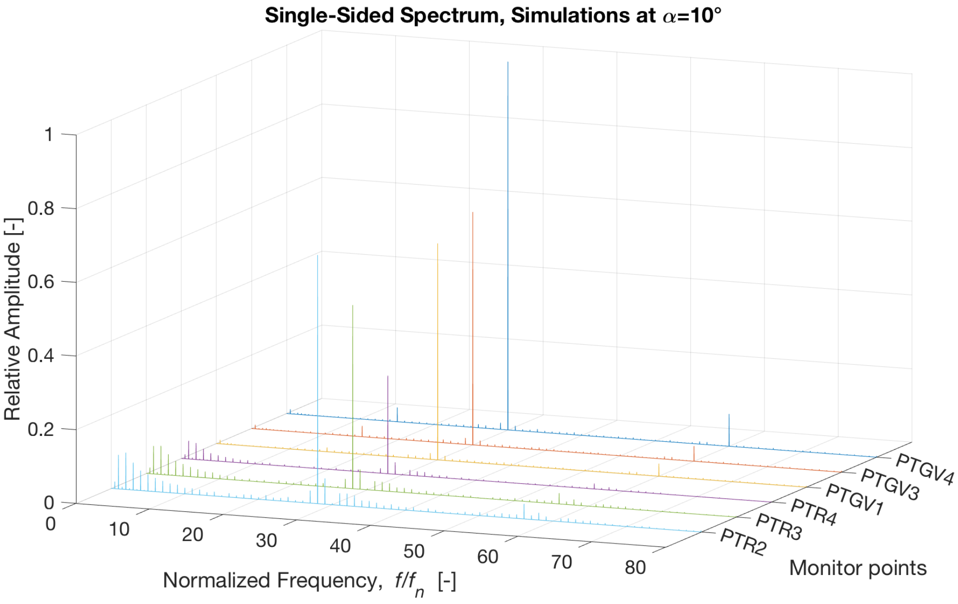

*Figure 4.20: Frequency spectrum for simulations at $\alpha = 10°$ at different monitor points.*

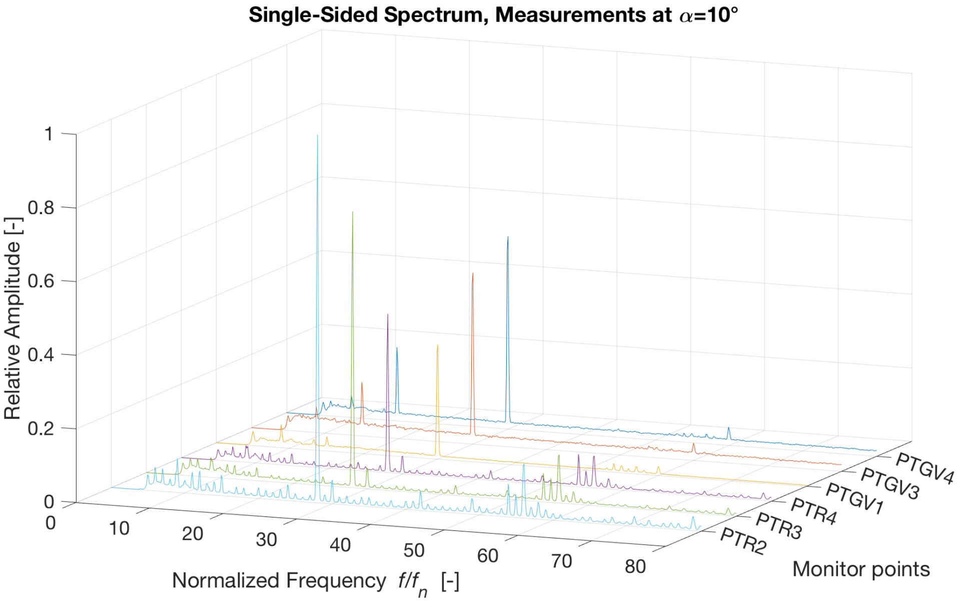

*Figure 4.21: Frequency spectrum for measurements at $\alpha = 10°$ at different monitor points.*

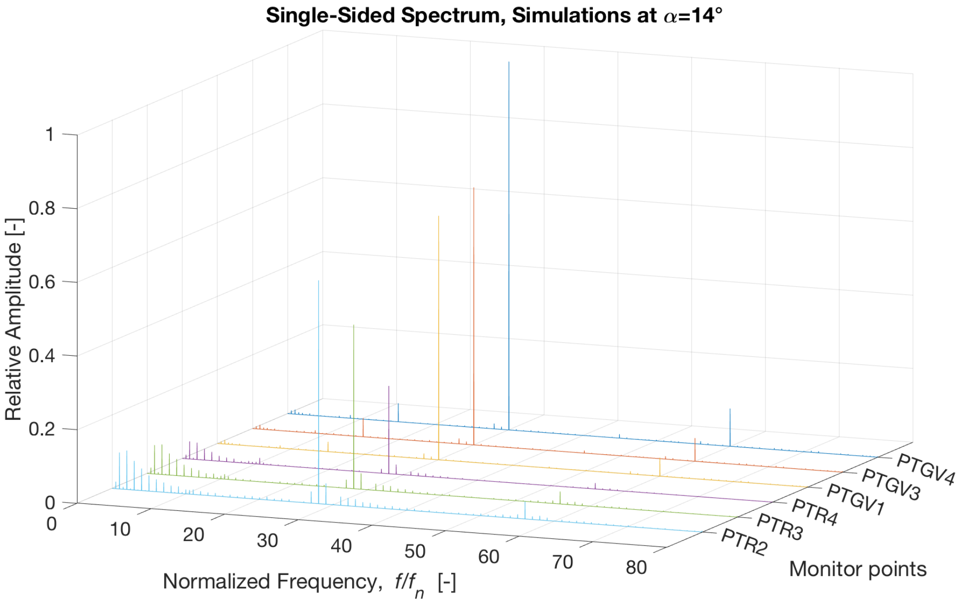

*Figure 4.22: Frequency spectrum for simulations at $\alpha = 14°$ at different monitor points.*

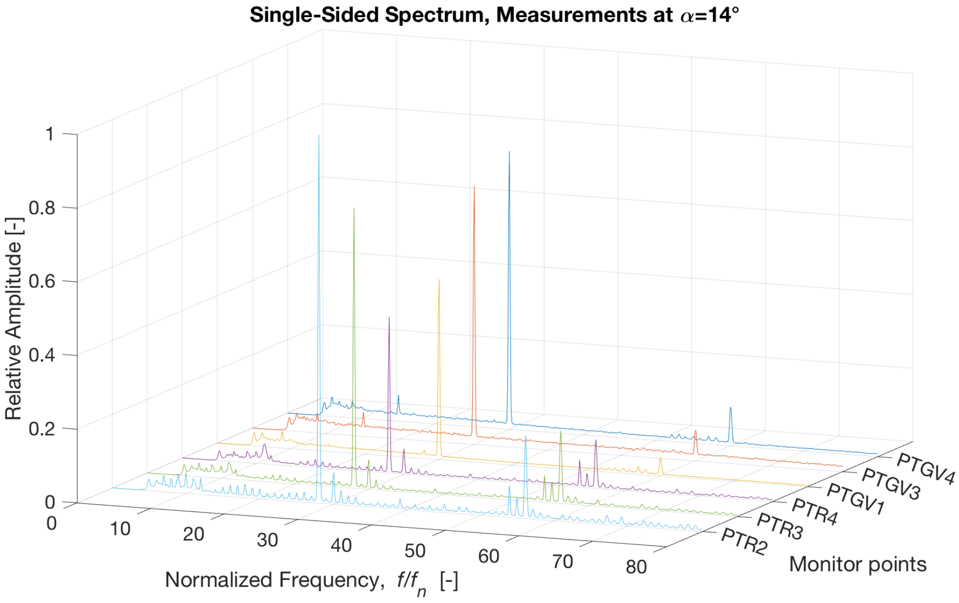

*Figure 4.23: Frequency spectrum for measurements at $\alpha = 14°$ at different monitor points.*

### 4.2.3 Amplitudes

While estimating the pressure peak-to-peak amplitudes for the experimental measurements requires using a Histrogram method or similar, the pressure curves from the simulations are periodic and the amplitude does not vary that much. Some approximate peak-to-peak amplitudes were therefore calculated in Matlab by finding the peaks and troughs of the simulation pressure curves, then finding the mean peak value and the mean through value, before subtracting the mean trough from the mean peak [3]. This is of course very simplified, but will give some indication of the amplitudes. In future amplitude calculations one should use histogram method on numerical results as well. The peak-to-peak amplitudes at PTR2, PTR4 and PTGV4 for selected values of alpha are compared to experimental results from Sannes in table 4.4. Sannes applied the histogram method with a 97 percent confidence level [34].

| | PTR2 | | PTR4 | | PTGV4 | |
|---|---|---|---|---|---|---|
| $\alpha$[°] | Sim. amp. [kPa] | Exp. amp. [kPa] | Sim. amp. [kPa] | Exp. amp. [kPa] | Sim. amp. [kPa] | Exp. amp. [kPa] |
| 4 | 2.384 | 4.196 | 0.949 | 5.769 | 3.330 | 2.957 |
| 7 | 2.545 | 2.860 | 1.005 | 1.624 | 3.630 | 2.872 |
| 10 | 2.651 | 3.042 | 1.046 | 1.671 | 3.928 | 2.361 |
| 12 | 2.925 | 3.043 | 1.142 | 1.657 | 4.834 | 2.563 |
| 14 | 3.419 | 3.425 | 1.343 | 1.928 | 5.650 | 3.214 |

*Table 4.4: Comparison of peak-to-peak amplitudes at PTR2, PTR4 and PTGV4.*

For both PTR2 and PTR4, the amplitudes are underpredicted. However, for the monitor point in the guide vanes, PTGV4, the amplitude is overpredicted. This confirms the observation from figure 4.17 through 4.23. It should be noted that the location of PTGV4 is located behind the trailing edge of the guide vanes as seen from figure 3.6, meaning that it is placed in the wake. This location is therefore not ideal for comparing amplitudes as the wake will affect the pressure variations due to the boundary layer effects. It should also be noted that the amplitude from the experiments at $\alpha = 4°$ for location PTR2 is very high according to table 4.4. Looking at the frequency spectrum in figure 4.12, this amplitude should not exceed that of $\alpha = 14°$. There is therefore some inconsistency in the results from the experiments. This could be explained by the fact that the peak-to-peak amplitudes of the measurements contain a lot more information than the simulations. In a laboratory setting, pressure oscillations will also arise from the hydraulic system, and these could affect the peak-to-peak amplitudes.

Jošt and Lipej did a study in order to predict the vortex rope. They found that differences in frequencies and amplitudes due to different time steps were negligible, but that the grid density affected the results. They found that the amplitudes of the pressure pulsations calculated using a fine grid resolution were significantly higher than those with a coarse grid. For a course grid at part load, the difference was 44 percent, but using a refined grid reduced this difference to less than 14 percent. Hence, the grid size is of great importance when evaluating the amplitudes. The difference in mesh resolution seen in figure 4.15 should therefore be avoided and is presumably the source of significant errors when estimating amplitudes in the guide vanes and runner. In doing future simulations, the meshes should be of more similar resolution to more accurately capture the relationship between the amplitudes in the two domains. Different time steps should also be considered in order to exclude that this has little effect on the amplitudes. In addition, one could try different turbulence models that capture the transient effects more accurately. Especially if the vortex rope is of interest the turbulence model is important. URANS (Unsteady Reynolds Averaged Navier Stokes) models can introduce excessive artificial dissipation in the flow, making it unable to reproduce the highly transient effects in a turbine. The Detached Eddy Simulation attempts to solve the turbulent eddies that are larger than the mesh resolution in a similar manner as in a Large Eddy Simulation (LES). Turbulent eddies that are smaller than the grid resolution are modelled in the same manner as in URANS. The dissipation term is modified in the DES model. Minakov et. al and Magnoli and Schilling both used DES in their simulations, both producing reasonable agreement with experimental results [8] [35]. A refined grid and a better turbulence model require more CPU-hours which increases the simulation costs.

(PAGE INTENTIONALLY LEFT BLANK)

# 5 | Further work

Because of the errors connected to the difference in grid density in the runner and the guide vanes, the number one priority is to create a mesh with better corresponding mesh resolution for the two domains. One should also consider including more of the draft tube in order to capture the vortex rope. Accurately predicting the vortex rope might however require a more advanced turbulence model as previous studies have shown that URANS is insufficient for this purpose [8].

When the mesh is satisfactory, the next step would be to perform simulations at not only different guide vane openings, $\alpha$, but also at different rotational speeds, $n$. One could then investigate whether operating the turbine at other speeds than synchronous speed is accurately predicted by simulations, and whether running the turbine at a different speed can reduce the pressure pulsations.

As a final step, when all simulations seem to correspond well with measurements, one could perform a Fluid-Structure Interaction (FSI) investigation in order to perform stress calculations and fatigue assessments.

(PAGE INTENTIONALLY LEFT BLANK)

# 6 Conclusion

Transient simulations for eleven different guide vane openings have been completed for the model turbine at the Waterpower Laboratory at NTNU. The frequency spectras for one point in the guide vanes, PTGV3, and one point in the runner, PTR2, have been obtained for all guide vane openings. The frequencies predicted by the simulations show good agreement with experimental measurements. The amplitudes also follow the same trend as the experiments when investigating a specific point at different guide vane openings. When keeping the guide vane opening constant and comparing points in the runner to points in the guide vanes, the frequencies also match well. However, the trend for the amplitudes in this case does not agree with experimental results. The simulations overpredict the amplitudes in the guide vanes compared to the amplitudes in the runner. This could be due to a difference in mesh resolution and should be further investigated. Further work will also include running simulations at different runner rotational speeds, $n$. It would also be interesting to include more of the draft tube in order to predict the flow downstream of the runner and maybe even find Rheingan's frequency. However, that might require more advanced turbulence modelling and will require more computational time as the simulations must run for more runner rotations in order for the vortex rope to stabilize.

(PAGE INTENTIONALLY LEFT BLANK)

# Bibliography

[1] americaslibrary.gov. *The World's First Hydroelectric Power Plant Began Operation.* URL: `http://www.americaslibrary.gov/jb/gilded/jb_gilded_hydro_1.html` (visited on 06/17/2018).

[2] W. J. Rheingans. "Power Swings in Hydroelectric Power Plants". In: *Transactions of the A.S.M.E.* 62.3 (Apr. 1940), pp. 171–184.

[3] Madeleine J. Selvig. "Numerical simulations of rotor-stator interactions at BEP for a high head Francis turbine". MA thesis. NTNU, 2017.

[4] Anup KC, Bhola Thapa, and Young-Hoo Lee. "Transient numerical analysis of rotor-stator interaction in a Francis turbine". In: *Renewable Energy* 65 (Oct. 2013).

[5] U. Seidel et al. "Dynamic loads in Francis runners and their impact on fatigue life". In: *OP Conference Series: Earth and Environmental Science* 22 (2014).

[6] L. Meng et al. "Study in the Pressure Pulsation inside Runner with Splitter Blades in Ultra-High Head Turbine". In: *IOP Conference Series: Earth and Environmental Science* 22 (2014).

[7] Dragica Jošt and Andrej Lipej. "Numerical Prediction of Non-Cavitating and Cavitating Vortex Rope in a Francis Turbine Draft Tube". In: *Strojniski vestnik - Journal of Mechanical Engineering* 57 (2011).

[8] M. V. Magnoli and R. Schilling. "Numerical simulation of pressure pulsations in Francis turbines". In: *IOP Conference Series: Earth and Environmental Science* 15 (2012).

[9] A. V. Minakov et al. "The numerical simulation of low frequency pressure pulsations in the high-head Francis turbine". In: *Computers Fluids* 111 (Feb. 2015).

[10] Xiao Yexiang et al. "Numerical analysis of unsteady flow under high-head operating conditions in Francis turbine". In: *Engineering Computations: International Journal for Computer-Aided Engineering and Software* 27.3 (Apr. 2010), pp. 365–386.

[11] Zhao Yaping et al. "Performance study for Francis-99 by using different turbulence models". In: *Journal of Physics: Conference Series* 579 (2015).

[12] Chirag Trivedi et al. "Experimental and Numerical Studies for a High Head Francis Turbine at Several Operating Points". In: *Journal of Fluids Engineering* 135.11 (Aug. 2013).

[13] U. Seidel et al. "Evaluation of RSI-induced stresses in Francis runners". In: *IOP Conference Series: Earth and Environmental Science* 15 (2012).

[14] International Electrotechnical Commission. *IEC 60193: Hydraulic turbines, storage pumps and pump-turbines – Model acceptance tests.* International standard. Geneva, Switzerland: International Electrotechnical Commission, 1999.

[15] Christoph Nicolet, Nicolas Ruchonnet, and François Avellan. "One-Dimensional Modeling of Rotor Stator Interaction in Francis Pump-Turbine". In: *23rd IAHR Symposium - Yokohama* (Oct. 2006).

[16] Chirag Trivedi, Michel Cervantes, and Ole Gunnar Dahlhaug. "Experimental and Numerical Studies of a High-Head Francis Turbine: A Review of the Francis-99 Test Case". In: *Energies* (Jan. 2016).

[17] Anup KC, Bhola Thapa, and Young-Hoo Lee. "CFD study on prediction of vortex shedding in draft tube of Francis tubrine and vortex control techniques". In: *Renewable Energy* 89 (Oct. 2016).

[18] Frank M. White. *Viscous Fluid Flow.* 3rd edition. New York, USA: McGraw-Hill Educations, 2006.

[19] Einar Kobro. "Measurement of Pressure Pulsations in Francis Turbines". Doctoral thesis: EPT, NTNU, Feb. 2010.

[20] Torbjørn K. Nielsen. *Dynamic Dimensioning of Hydro Power Plants.* NTNU. 1990.

[21] Hu Ying et al. "Numerical simulation of unsteady turbulent flow through a Francis turbine". In: *Wuhan University Journal of Natural Sciences* 16 (Apr. 2011).

[22] Sigma2. *Uninett Sigma2.* URL: `https://www.sigma2.no/` (visited on 06/04/2018).

[23] Norwegian Hydropower Centre. *Francis-99.* June 2018. URL: `https://www.ntnu.edu/nvks/francis-99` (visited on 06/20/2018).

[24] Ken-Robert G. Jakobsen and Martin Aasved Holst. "CFD simulations of transient load change on a high head Francis turbine". In: *Journal of Physics: Conference Series* 782 (2017).

[25] sharcnet.ca. *Set Up Periodicity.* 2015. URL: `https://www.sharcnet.ca/Software/Ansys/17.0/en-us/help/icm_help/imesh_periodicity.html` (visited on 04/16/2018).

[26] F. R. Menter. "Two-Equation Eddy-Viscosity Turbulence Models for Engineering Applications". In: *AIA A Journal* 32.8 (Aug. 1994).

[27] sharcnet.ca. *5.4.3. GGI (General Grid Interface) Connections.* 2015. URL: `https://www.sharcnet.ca/Software/Ansys/16.2.3/en-us/help/cfx_mod/CACBCJBF.html` (visited on 02/28/2018).

[28] sharcnet.ca. *5.3.3. General Connection.* 2015. URL: `https://www.sharcnet.ca/Software/Ansys/17.0/en-us/help/cfx_mod/CACDIGEH.html` (visited on 02/28/2018).

[29] Chirag Trivedi, Bhupendra Gandhi, and Cervantes J. Michel. "Effect of transients on Francis turbine runner life: a revie". In: *Journal of Hydraulic Research* 51 (2013), pp. 121–132.

[30] Larry Hardesty. *Explained: The Discrete Fourier Transform.* 2009. URL: `http://news.mit.edu/2009/explained-fourier` (visited on 02/28/2018).

[31] G. Heinzel, A. Rüdiger, and R. Schilling. "Spectrum and spectral density estimation by the Discrete Fourier transform (DFT), including a comprehensive list of window functions and some flat-top windows". In: *Teilinsitut, Max-Planck-Institut für Gravitationsphysik (Albert-Einstein-Institute)* (2002). Hannover, Technical report.

[32] Z. U. A. Warsi Joe E. Thompson and C. Wayne Mastin. *Numerical Grid Generation, Foundations and Applications.* Elsevier Science Publishing Co., Inc., 1985.

[33] Christopher J. Freitas. "The issue of numerical uncertainty". In: *Applied Mathematical Modelling* 26.2 (Feb. 2002).

[34] Daniel B. Sannes. "Pressure pulsation and Stresses in a Francis turbine operating at Variable Speed". Master thesis. NTNU, June 2017.

[35] A. V. Minakov et al. "Numerical modeling of flow in the Francis-99 turbine with Reynolds stess model and detached eddy simulation method". In: *Journal of Physics: Conference Series* 579 (2015).

[36] MathWorks. *Filter Builder Design Process.* URL: `https://www.mathworks.com/help/signal/ug/filterbuilder-design-process.html#responsive_offcanvas` (visited on 06/06/2018).

(PAGE INTENTIONALLY LEFT BLANK)

# APPENDIX A:
# Procedures in ANSYS and MATLAB

## A.1 ANSYS procedure

This appendix provides a description for the procedure used in ANSYS and CFX.

### A.1.1 ICEM

It is assumed that a guide vane mesh has already been provided, and that the task is to turn the guide vane into the correct position.

- Turn both geometry and blocking into the desired position. It is only necessary to turn one guide vane if the mesh provided is periodic. This guide vane will be turborotated in CFX later. Make sure that all associations are updated.
- Check quality of mesh. If the quality is satisfactory, export the mesh for CFX. If the quality is not satisfactory, move vertices to get better mesh quality before exporting to CFX.

### A.1.2 CFX

It is assumed that runner mesh and draft tube mesh is provided.

**CFX Pre**

- Import meshes for the runner, guide vanes and draft tube. Copy and turborotate guide vanes and runner blades around the rotation axis.
- Set up domains and interfaces for the runner, guide vanes and draft tube.
- Specify appropriate boundary conditions.
- Add the desired monitor points.
- Set up analysis for either transient or steady state with desired criterias.
- Set up backup. Optional for transient: Set up desired transient results.
- Write solver input file.

**CFX Solver**

- Set up solver run from the input file. Transient only: Use steady state results as initial values.
- Transient only: Export pressure variables from the finished run into a table, such as csv. These are used for the analysis in MATLAB.

## A.2 MATLAB procedure

- Import pressure variables from the csv-file.
- Use bandpass filter to let through desired frequencies and bandstop filter to remove undesireable frequencies. Make sure that attenuation does not affect the ratio between the amplitudes too much. The filterBuilder design process is thoroughly described in MATLAB's documentation [36].
- Perform an FFT on the signal.
- Present data in appropriate form.

# APPENDIX B:
# Paper for CRHT-VIII’18

The following paper was written in association with CRHT-VIII’18 symposium in Kathmandu, Nepal.

# Pressure pulsations in high head francis turbines

**M J Selvig, O G Dahlhaug and C Trivedi**

Department of Energy and Process Engineering,Norwegian University of Science and Technology, Trondheim, Norway

**Abstract.** As energy demand is growing along with the quest for green energy, the operating range for hydropower is being pushed into non-favourable conditions. The unsteady flow regimes at these conditions lead to transient phenomena's like pressure oscillations that can propagate through the whole turbine, threatening the reliability of the turbine. It is therefore important to identify these pressure pulsations to ensure safe operation. This paper presents the preliminary work of a master thesis at the Norwegian University of Science and Technology (NTNU). Transient simulations of the Francis model turbine at the waterpower laboratory are to be performed at ten different guide vane openings ranging from a 4-degree opening to a 14-degree opening. The software used for the simulations is ANSYS CFX 18.1, applying the SST turbulence model. The primary focus is rotor-stator interactions (RSI), hence the model has been simplified accordingly, limiting the computational domain to guide vanes, runner and part of the draft tube. The frequency spectrum is to be obtained at several monitor points in the domain through Fast Fourier Transformations (FFT) in Matlab. The simulation results are subsequently compared to experimental values for verification.

## 1. Introduction

As energy demand is growing along with the quest for green energy, the requirement for flexibility in hydropower is being pushed to its limits. Together with frequent changes in consumption patterns from moment to moment, hour to hour, day to day and season to season, adjusting the energy production in real-time is becoming increasingly more important. The introduction of solar- and wind energy is driving this concept even further, the turbine is forced to operate at conditions for which it was not designed, leading to transient phenomena's like pressure pulsations that threatens the reliability of the turbine.

With the advancement in computer technology, Computational Fluid Dynamics (CFD) has emerged as a powerful tool for evaluating the performance of turbines. Turbines are tailor-made to specific conditions on a specific site, and small improvements in the geometry can have a large positive effect on operation [1]. Identifying problem areas is therefore very important. CFD simulations based on individual components in a turbine are common. Anup et al. did simulations of a Francis turbine and tested two techniques for minimizing vortex shedding downstream of the runner, both of them only moderately successful [2]. Minakov et al. showed that that low-frequency pressure pulsations in water turbines are mainly caused by the vortex rope. The results corresponded well with experimental data for pulsational characteristics [3]. Already in 1940, Rheingan had shown that the vortex rope could cause power swings, and identified the so-called Rheingan's frequency [4]. Jošt and Lipej looked at pressure pulsation amplitudes at different guide vane openings and compared the results with experimental data. While the frequencies they obtained were close to the experimental ones, the amplitudes were less accurate. Better results for amplitudes were however obtained with a refined grid [5]. KC et al. did a numerical analysis on Rotor-Stator interactions (RSI) in a Francis turbine and revealed two dominating frequencies, the runner speed frequency and the guide vane frequency [1]. Nicolet et al. presented an approach for modelling the hydroacoustic part of RSIs and found that the guide vane wave speed and runner rotating frequency strongly influence the amplitude of the standing wave [6]. Simulations of the entire flow passage of the turbine is gaining more interest as computational time and costs are cut. Magnoli and Schilling did a numerical simulation of a prototype turbine and that agreed well with experimental results, and found that extreme operating conditions were the most computational heavy [7]. Ying et al. [8] and Yexiang et al. [9] used numerical simulations of the whole turbine to verify that each component was designed reasonably.

Flow in reaction turbines is three dimensional, rotational due to the change in flow direction, turbulent and unsteady [1]. Another important attribute when looking at dynamic forces is the turbine's transient behaviour. While steady state analysis can predict efficiency, cavitation and hydraulic losses, a transient analysis is necessary in order to capture pressure pulsations [1].

This paper presents the preliminary work for numerical predictions of pressure pulsations in the high head Francis turbine at the Water Power Laboratory at NTNU at several operating points through CFD simulations. The simulations are then to be compared to experimental results. It should be noted that the transient results in this paper for the Best Efficiency Point (BEP) with $\alpha$=9.84 degrees are compared to experimental measurements from 2014, while the new steady state results for $\alpha$=9, 8, 7 and 6 degrees are verified against new measurements. These two results should be considered separately.

## 2. Theory

### *2.1. Rotor-stator-interaction*

Pressure oscillations in fluid flow is a transient phenomena that impacts the mechanical structure of the turbine. Rotor-stator-interaction (RSI) is the main cause behind pressure pulsations during normal operation at full load. [7] A steady state analysis is less time consuming than a transient analysis, and while it can predict performance parameters like efficiency, cavitation and hydraulic losses, analysing dynamic forces requires the calculation of unsteady flow with advanced turbulence models.

RSI results from the interaction between the rotating flow perturbations by the runner blades, and the perturbations in the flow from the guide vanes [6], thus it is associated with the blade passing frequency and guide vane frequency. The blade passing frequency, $f_{BP}$, is determined by the number of runner blades, $Z_{BP}$, and runner rotation frequency, $f_n$.

$$f_n = \frac{n}{60} \quad [Hz] \tag{1}$$

$$f_{BP} = f_n \cdot Z_{BP} \cdot m \quad [Hz] \tag{2}$$

Here n is the rotational speed in rpm, $Z_{BP}$, is the number of runner blades, while $m=1, 2, 3\ldots$, representing different harmonics. The gate passing frequency, or guide vane frequency, is calculated from

$$f_{GV} = f_n \cdot Z_{GV} \cdot m \quad [Hz] \tag{3}$$

where $Z_{GV}$ is the number of guide vanes and $m=1, 2, 3\ldots$. According to Seidel et al., higher harmonics have very little impact on Francis runners [10], hence $m=1$ is the most significant frequency.

RSI produces pressure waves that propagate through the whole turbine. The interaction between runner and guide vanes causes pulsations at the runner inlet based on two phenomenas:
1) A rotating observer passes the wake of all guide vanes during a full rotation.
2) Every time a runner blade passes a guide vane, a pressure pulse is generated [10].
As the guide vane angle is changed, the amplitude of the frequency of the pressure pulse will vary. The most significant fluctuations arise when the trailing edge of the guide vanes are close to the runner blades. Increased distance between stator and rotor blades will increase turbulence mixing and dissipate wakes and thereby decrease RSI effects. Because low and medium head Francis units have a larger distance between rotor and stator, RSI-induced phenomena's are negligible. Pressure fluctuations caused by RSI's in the high head units are therefore most critical and can cause stability problems [10].

The flow field leaving the guide vane of a Francis turbine is characterized by the velocity irregularity caused by the guide vanes. The pressure field caused by the runner blade also induces flow field distortions. These periodic flow fields can both be represented as Fourier series, and can for the stationary and rotating pressure fields be expressed as:

$$p_s(\theta_s, t) = \sum_{n=1}^{\infty} B_n \cos\left(nZ_{GV}\theta_s + \varphi_n\right) \tag{4}$$

$$p_r(\theta_r, t) = \sum_{m=1}^{\infty} B_m \cos\left(nZ_{BP}\theta_r + \varphi_n\right) \tag{5}$$

A modulation process combines the two pressure fields into a resulting pressure field. The pressure in the vaneless gap can be expressed as the product of both the rotating and stationary pressure fields. By using the identity for circular functions and the relation between the runner angle coordinate to the stationary system of reference, $\theta_r=\theta_s-\omega t$, the pressure field in stationary coordinates becomes:

$$\begin{aligned} p_{mn} &= \frac{A_{mn}}{2}\cos(mZ_{BP}\omega t - (mZ_{BP} - nZ_{GV})\theta_s + \varphi_n - \varphi_m) \\ &+ \frac{A_{mn}}{2}\cos(mZ_{BP}\omega t - (mZ_{BP} + nZ_{GV})\theta_s - \varphi_n - \varphi_m) \end{aligned} \tag{6}$$

for $m=1,2,\ldots\infty$ and $n=1,2,\ldots\infty$. Equation 6 describes the pressure field in the vaneless gap. Here $A_{mn}$ is the combined pressure amplitude due to the interaction of each harmonics. The numbers of minima and maxima for the two diametrical pressure modes is given by:

$$k_1 = mZ_{B\square} - nZ_{GV} \tag{7}$$

$$k_2 = mZ_{BP} + nZ_{GV} \tag{8}$$

with a rotational speed in the stationary frame of reference:

$$\omega_1 = \frac{mZ_{BP}\omega_b}{k_1} \tag{9}$$

$$\omega_2 = \frac{mZ_{BP}\omega_b}{k_2} \tag{10}$$

The RSI patterns are thereby determined by the relations in table 1 [6].

|  |  |  |  | **Stationary frame** |  |  | **Rotating frame** |  |  |
|---|---|---|---|---|---|---|---|---|---|
| $m$ | $n$ | $k_1$ | $k_2$ | $\omega_1/\omega_b$<br>$mZ_{BP}/k_1$ | $\omega_2/\omega_b$<br>$mZ_{BP}/k_2$ | $f/f_n$<br>$mZ_{BP}$ | $\omega_1'/\omega_b$<br>$nZ_{GV}/k_1$ | $\omega_2'/\omega_b$<br>$nZ_{GV}/k_2$ | $f/f_n$<br>$nZ_{GV}$ |
| 1 | 1 | 2 | 58 | 15 | 0.51 | 30 | 14 | 0.48 | 28 |
| 1 | 2 | -26 | 86 | -1.15 | 0.34 | 30 | -2.15 | 0.65 | 56 |
| 2 | 2 | 4 | 116 | 15 | 0.51 | 60 | 14 | 0.48 | 56 |
| 2 | 3 | -24 | 144 | -2.5 | 0.41 | 60 | -3.5 | 0.58 | 84 |
| 3 | 3 | 6 | 174 | 15 | 0.51 | 90 | 14 | 0.48 | 84 |
| 3 | 4 | -22 | 202 | -4.09 | 0.44 | 90 | -5.09 | 0.55 | 112 |
| 4 | 4 | 8 | 232 | 15 | 0.51 | 120 | 14 | 0.48 | 112 |
| 5 | 5 | 10 | 290 | 15 | 0.51 | 150 | 14 | 0.48 | 140 |
| 13 | 1 | -2 | 782 | -195 | 0.49 | 390 | -196 | 0.50 | 392 |

**Table 1:** Expected frequencies and diametrical modes. Based on [6] with values from [11].

It should be mentioned that the turbine has splitter blades, and that this will affect the pressure pulsations from RSI. Splitter blades extend the efficiency region and decrease pressure pulsations. Meng et al. found that for an ultra-high head Francis unit with 16 main blades and 16 splitter blades, the amplitude of the blade passing frequency was higher with increasing length of the splitter blades. They also found that the amplitude of the pressure pulsations in the whole turbine was the smallest when the length ratio of the splitter blades was 0.825 of the main blades [12].

### *2.2. The vortex rope*

At part load, the oscillations originate mainly from the vortex rope in the draft tube [7]. The purpose of the draft tube is to reduce the exit velocity of the flow in order to minimize loss of kinetic energy and recover energy at the outlet. The flow leaving the runner under optimal conditions has no rotational component of velocity and is virtually axial. During part load or high load operation, the exiting flow contains a swirl component that generates a vortex at the centre of the flow downstream of the runner. Excessive swirl leads to instabilities that introduce pressure fluctuations and eventually the draft tube surge. A helical vortex, the vortex rope, is characteristic of the draft tube surge. This flow is self-excited unsteady because the flow within the draft tube varies with time, while the discharge from the draft tube may or may not vary with time [2]. The vortex rope can cause serious problems for hydraulic equipment as powerful flow pulsations lead to strong vibrations of the turbine structure. Resonance can even lead to turbine structural failure [3]. The draft tube vortex frequency, or Rheingans frequency [4], is given by

$$f_R \cong \frac{f_n}{3.6} \quad [Hz] \tag{4}$$

Simulation of the vortex rope is very time consuming. It takes considerable time for the frequency of the vortex rotation to stabilize and for the vortex to assume its final shape. According to Jošt and Lipej, as much as 40 runner revolutions is usually necessary in order to get stable values for pressure pulsation frequency and amplitudes [5]. Yexiang et al. ran simulations for 3600 time steps in order to capture the vortex rope [9]. This is well beyond the resources available, hence the focus is therefore on RSIs.

### *2.3. Vortex shedding*

For almost any bluff body, vortex shedding starts at approximately Re>35, and persists over a wide range of Reynolds numbers. Vortex shedding is the separation that occurs in the wake of the body, with pairs of vortices alternately shed from the upper and lower part of the rear surface. The wake becomes more turbulent and complex with increasing Reynolds numbers, but can still be detected at Re=$10^7$ [13]. Vortex shedding can cause fatigue failure of the stay vanes in Kaplan turbines. It can also cause noise from the trailing edges of the runner blades in Francis turbines, indicating that the trailing edges need modification [14].

### 2.4. Other pressure fluctuations

Some pressure fluctuations can arise from inequalities in the system, for example if a steady flow of water is interrupted by a sudden closing of the main valve, or even a change in the guide vane position. These fluctuations are independent of the rotational speed of the turbine, but depend on the geometry of the waterway and the propagation speed of the pressure wave, i.e. the speed of sound in water. These pressure fluctuations are due to the elasticity of the water and are known as the water hammer [15].

### 2.5. About the turbine

The model turbine at the waterpower laboratory at NTNU is a Francis type turbine. It includes a spiral casing, a distributor with 14 stay vanes integrated into the spiral casing and 28 guide vanes. The runner has 15 blades with an additional 15 splitters. The draft tube is an elbow-type. The test rig at the waterpower laboratory is a hydraulic system capable of generating ≈12 m head for open loop, and ≈30 m head for closed loop [11].

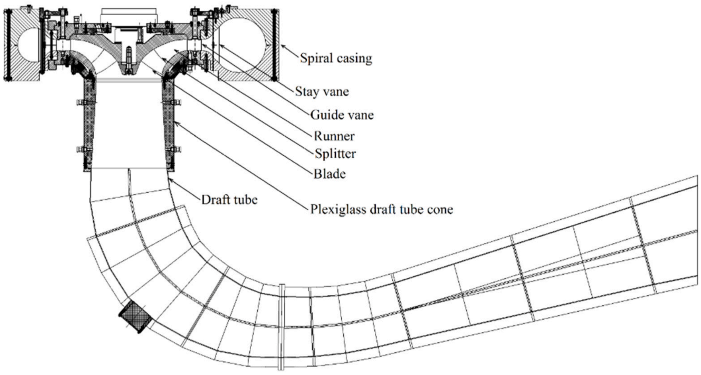

**Figure 1.** 2D view of the turbine model. Retrieved from **[11]**.

### 2.6. Turbulence modelling

Flow in a hydraulic turbine is swirling and very turbulent. Because of very small turbulence scales, like the Kolmogorov microscales, it is very time-consuming and computational heavy to solve all scales because it would require a very fine computational mesh. In order to cut computational time, turbulence modelling is therefore necessary. The choice of turbulence model is important because the calculated results will differ depending on the model chosen [5] [8]. According to a study by Magnoli and Schiller, turbulence modelling is crucial for a proper turbine flow simulation [7]. However, when looking at the draft tube only, Jošt and Lipej found that when cavitation is not modelled, the solutions were independent of the turbulence model [5].

Which turbulence model to apply relies on the subject at hand. According to Thapa et al, the Shear stress model (SST), realizable k-ε model and standard k-ε model is sufficient when analysing RSI and pressure pulsations. If the vortex rope is to be predicted, turbulence models such as RNG k-ε, SAS-SST or LES will give more accurate results. But these will in turn require a finer grid and larger computational effort and thereby simulations take longer time [1].

## 3. Model description

### *3.1. Computational domain*

Because the flow in the different turbine components are connected and interact with one another, individual component analysis does not correspond correctly to the experimental data. A full analysis on the turbine with spiral casing, distributor, runner and draft tube is necessary, according to Magnoli and Schilling, for a complete simulation of the flow through the turbine [7]. This is very time consuming. Because time is a limiting factor, a simulation of the turbine as a whole is not feasible. Hence, the focus is on the interaction between the guide vanes and runner. The computational domain has therefore been limited to guide vanes, runner and part of the draft tube. Because the draft tube is quite large, it requires a lot of cells. Reducing the draft tube into only a small section thereby saved a lot of computational time by reducing the domain substantially. The guide vanes and runner have strong influence on one another because of dynamic forces, and the pressure pulsations from RSIs are very prominent in high head units. Seidel et al. showed that the gate passing frequency was the dominating frequency for a high head Francis unit, and that fatigue life therefore was governed nearly exclusively by RSIs [1] [10]. The entire computational domain then consisted of three main components: guide vanes, runner and part of the draft tube as can be seen from figure 2. It was also assumed that no leakage occurs.

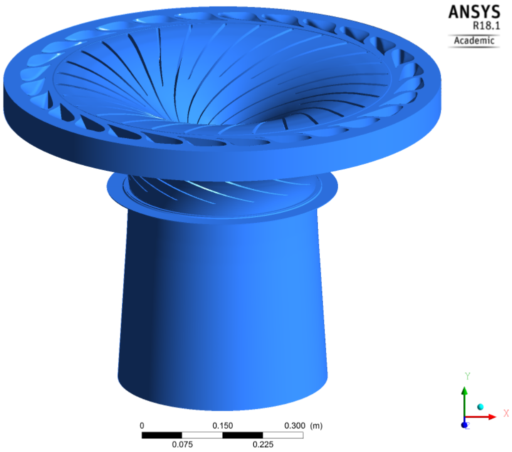

**Figure 2.** An overview of the whole flow passage.

The entire fluid domain was formed in CFX by combining the components with an interface between the guide vanes and runner, and an interface between runner and draft tube, using GGI (General Grid Interface) as grid connection for both mesh connections. GGI permits a connection where the connected surfaces does not match [16]. A rotating domain was set up for the runner in CFX Pre, while stationary domains were set up for guide vanes and draft tube. Frozen Rotor model was chosen as the connection between guide vanes and rotor for the steady state simulations. Using Frozen Rotor approach, the frame of reference is changed, but the relative components across the surface is fixed. It produces a steady state-solution with some account of the interaction between the two frames of reference. This approach is the least computational heavy of the three models to choose from in ANSYS. However, transient effects are not captured with Frozen Rotor, meaning that for transient simulations another connection type had to be used. The Transient Rotor-Stator was used for those simulations because it can predict the transient interaction between a stator and a rotor passage as it accounts for all interaction effects between components that are moving relative to one another. The downside is that this model is computational heavy and require a lot of disk space [17].

The location of the monitor points was provided by EDR Medeso for BEP as their meshes and geometries were used. These are presented in figure 3. This is not the coordinate system or guide vane mesh used for other values of α, and the location of the monitor points is somewhat different for those analyses.

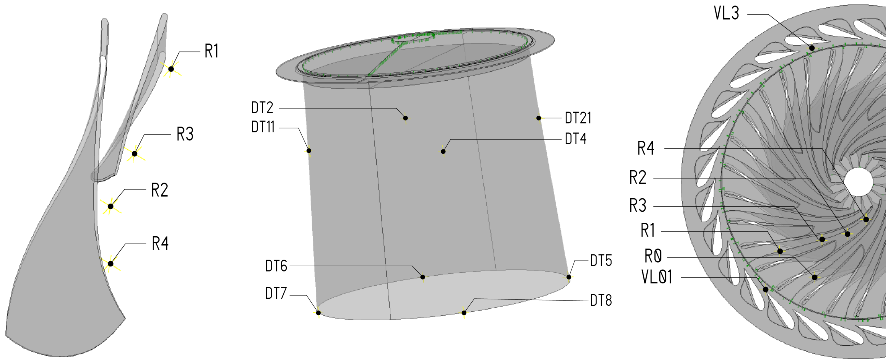

(a) (b) (c)

**Figure 3.** Monitor points and their location in one runner passage (a), draft tube (b) and vaneless gap (c).

### *3.2. Boundary conditions*

In addition to choosing a turbulence model, reasonable boundary conditions have to be determined. [18]

- **Inlet**
    - Volumetric flow is used as inlet condition. The flow direction is angled as if the water is leaving the stay vanes. This was achieved by applying vectors in cylindrical coordinates.
- ***Outlet***
    - A static pressure of 0 Pa (relative to 1 atm) is used as outlet condition. The pressure is unknown at the outlet, but because the Navier Stokes equation calculates pressure difference, setting the exact value of the pressure at the outlet is not crucial when investigating pressure fluctuations. This leads to negative absolute pressure at some locations, which is physically impossible, but the pressure difference is correct nonetheless, which makes this assumption acceptable for this case.
- **Close to walls**
    - No slip condition is applied at solid walls. This means that $u=v=w=0$ along solid walls where $u$, $v$ and $w$ is the velocity components in the three directions of the coordinate system.
- **Initial values**
    - Steady state results were used as initial values.
- **Time step**
    - In their numerical analysis of RSI, KC et al. [1] used a time step that corresponded to a $2^{\circ}$ rotation of the runner, that is 0.00037037 s for a case where the rotation rate n=900 rpm. In that case, the runner had 13 blades, which means that they would have approximately 14 points between each time a runner blade passes a guide vane. For the case of the runner in the waterpower laboratory, a $2^{\circ}$ rotation of runner would correspond to 12 points between each time a runner main blade is passing a guide vane, and a time step of 0.00099365 s at BEP. With only 12 points, there would be little information to retrieve the fundamental frequency from, and perhaps even impossible to find the second harmony. Hence it is reasonable to choose a smaller time step. It was therefore decided to use a time step of 0.000477 seconds, corresponding to 25 points between each main blade passing a guide vane, yielding 12,5 points between a main blade and a splitter blade.

### *3.3. Software and hardware*

The CFD simulations were carried out with ANSYS CFX version 18.1. The computer available for simulations had an Intel Xeon E5-1650 processor with six cores and 64 GB RAM. This is far from ideal for transient simulations, but it was sufficient for the analysis to run even though it took a great deal of time.

### *3.4. Mesh*

The mesh for the runner, guide vanes at BEP and the upper part of the draft tube was provided by EDR Medeso. Because no geometry was provided for the guide vanes, another mesh was used for further analyses at different guide vane openings other than BEP in order to be able to turn the guide vanes into the correct position. The geometry, blocking and mesh for this was provided by Chirag Trivedi, and then modified in ICEM in order for it to fit together with the runner mesh. The outlet from the guide vanes was lengthened by 1.5 mm as well as increasing the distance between hub and shroud side by 0.8 mm. Mesh statistics are listed in the table 3.

| Domain | Number of elements | Number of nodes |
|---|---|---|
| **Draft tube** | 4494400 | 3393125 |
| **Guide vanes** | 7948080 | 8353968 |
| **Runner** | 9220050 | 9664035 |
| **Total** | 21662530 | 21411128 |

**Table 2.** The number of elements and nodes for the different domains at $\alpha$=9 degrees, and the entire flow passage. The same amount applies for all other guide vane openings, except for BEP because of a different guide vane mesh.

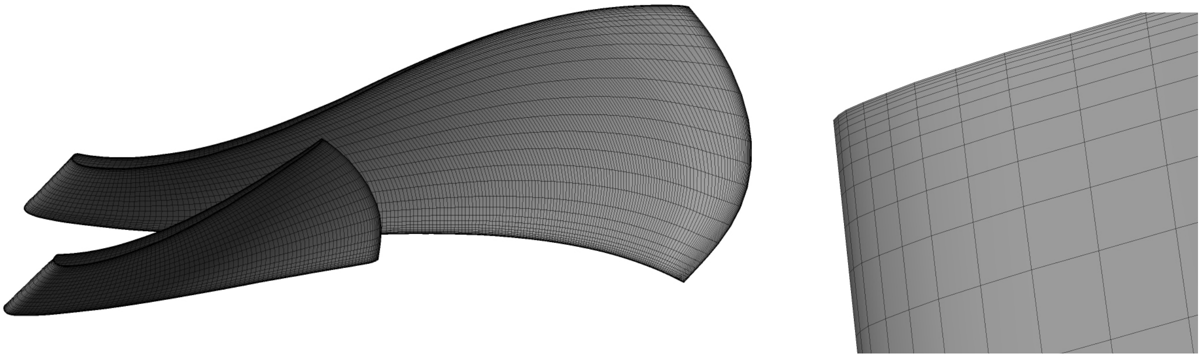

**Figure 4.** To the left is the mesh for the main blade and the splitter blade. To the right is a close-up of the leading edge of the main blade. The mesh is refined close to edges.

All meshes have previously been used in similar CFD simulations where grid convergence tests was performed. Such tests was therefore not done for this paper.

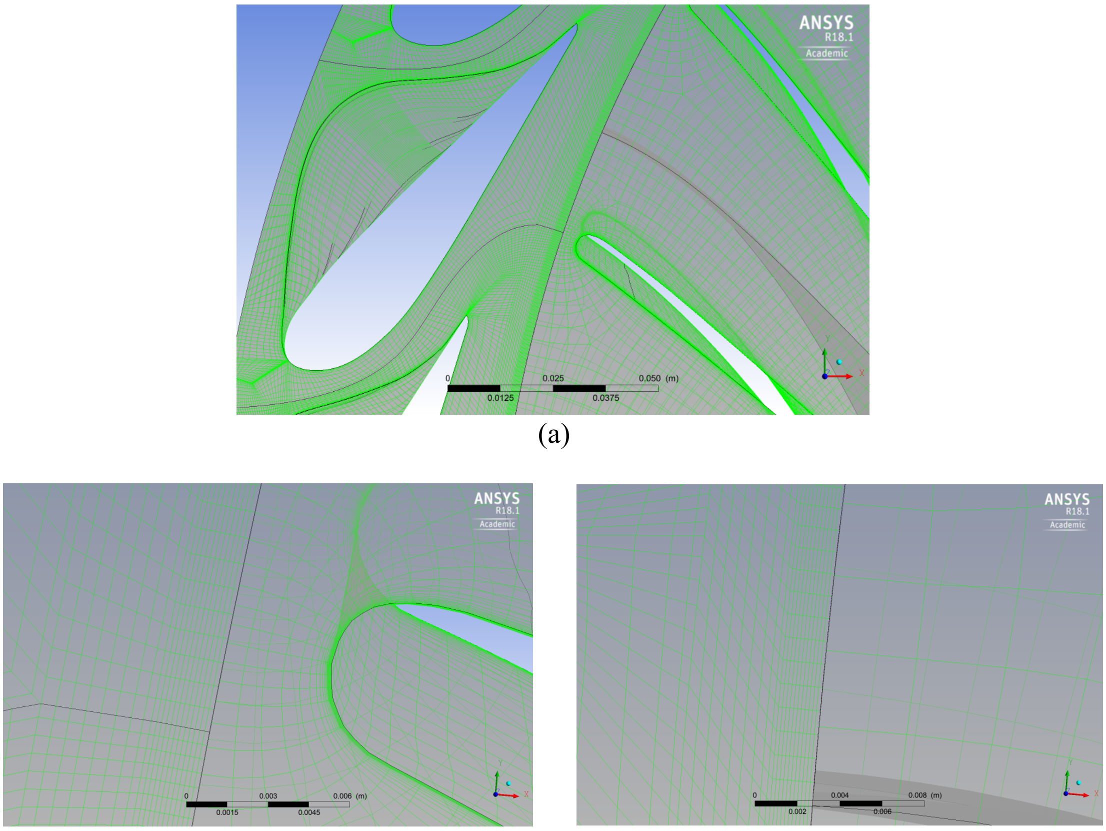

(a)

(b) (c)

**Figure 5.** Figure (a) shows the modified mesh for the guide vanes at α=9 degrees together with the runner. It can be seen from figure (b) that there is a large difference in cell size from guide vane to runner. This becomes even more evident in the runner passages as seen in figure (c).

### *3.5. Turbulence model*

The SST model was used for simulations because it can provide a good estimate both close to walls and in the free stream. The SST turbulence model is an industry standard and uses the k-ω model close to the wall, but because that model is sensitive to the inlet free stream turbulence properties, it utilises the k-ε model in the free stream. SST is merited for good performance in adverse pressure gradients and separating flow [1] [19]. The SST model is expressed mathematically as:

$$\frac{D\rho k}{Dt} = \tau_{ij}\frac{\partial u_i}{\partial x_j} - \beta * \rho \omega k + \frac{\partial}{\partial x_j}\left[(\mu + \sigma_k \mu_t)\frac{\partial k}{\partial x_j}\right] \tag{6}$$

$$\frac{D\rho\omega}{Dt} = \frac{\gamma}{\nu_t}\tau_{ij}\frac{\partial u_i}{\partial x_j} - \beta\rho\omega^2 + \frac{\partial}{\partial x_j}\left[(\mu + \sigma_\omega \mu_t)\frac{\partial \omega}{\partial x_j}\right] + 2(1 - F_1)\rho\sigma_{\omega 2}\frac{1}{\omega}\frac{\partial k}{\partial x_j}\frac{\partial \omega}{\partial x_j} \tag{7}$$

### *3.6. Frequency analysis*

In order to identify the different frequencies from the simulations, the data obtained has to be processed. The Fourier transform transforms a periodic signal from the time domain to the frequency domain. It is a way to decompose an otherwise erratic signal into their constituent frequencies [20]. The Discrete Fourier Transform (DFT) is used when working with discrete data. The practical implementation of DFT on a computer, however, is often the Fast Fourier Transform (FFT) algorithm [21]. The FFT is a built in function in Matlab. The scripts used for processing the simulation results and experimental measurements are given in the appendix.

### *3.7. Steady state analysis*

The first step in order to get the transient results was to get a working steady state solution. A steady state run was performed with a convergence criteria of RMS $< 10^{-4}$. This results file was used as initial conditions for the transient simulations. The steady state simulation at BEP ran for 700 iterations without reaching the convergence criteria. It was, however, apparent that that the simulation had converged sufficiently because the curves for the pressure at the monitor points showed little variation, even though some RMS values still were above $10^{-4}$. Even so, a low quality steady state results file would cause the transient analysis to converge slower, but should yield correct results nonetheless. The transient simulation at BEP would converge after three inner loop iterations.

For an alpha of 7, 8 and 9 degrees, the solver reached the convergence criteria after approximately 150 iterations. At $\alpha$=6 degrees the solver ended after 1000 iterations without having reached the criteria. Again, the solution showed little variation in pressure at the monitor points, and the solution was presumed sufficient for further analyses.

### *3.8. Transient analysis at BEP*

The transient simulation at BEP was carried out for 1126 time steps, corresponding to three runner revolutions. One runner revolution took approximately two days to complete. As the results varied very little already during the first runner revolution, both the second and third revolution was used for the frequency spectrum analysis because a larger data set yields a more accurate solution.

## 4. Preliminary results

### *4.1. Steady state results*

In order to run transient analyses, a steady state file is needed as input for initial values. To verify that the steady state results are reliable, the torque and efficiency has been compared to experimental measurements for $\alpha$ equal to 6, 7, 8 and 9 degrees as listed in table 3. The smallest deviation from experimental measurements for both torque and efficiency is at $\alpha$=9 degrees, with a deviation of 4.1% for torque and 3.3% for efficiency. The difference from experimental measurements increases as the operation point move further away from BEP, with the largest difference observed at $\alpha$=6 degrees, with a difference of 9.3% and 4.2% for torque and efficiency respectfully.

| Alpha | Experiments | | Simulations | |
|---|---|---|---|---|
| | Torque (Nm) | Efficiency (%) | Torque (Nm) | Efficiency (%) |
| 6 | 385.9 | 89.7 | 421.9 | 93.5 |
| 7 | 451.5 | 91.1 | 477.8 | 94.4 |
| 8 | 512.6 | 91.8 | 536.3 | 95.0 |
| 9 | 574.5 | 92.3 | 598.3 | 95.3 |

**Table 3.** Comparison of measured results and numerically obtained results.

The pressure contours for the steady state simulations show areas of negative pressure because of the outlet condition of 0 Pa. This is nonphysical and impossible, but the pressure difference should be correct nonetheless and it is possible to identify areas of low and high pressure.

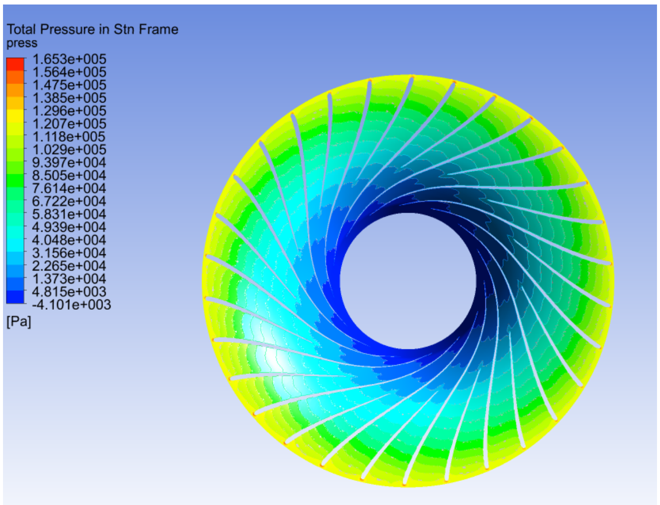

**Figure 6.** Contour of total pressure in a stationary frame in the runner for steady state simulation at α=9 degrees.

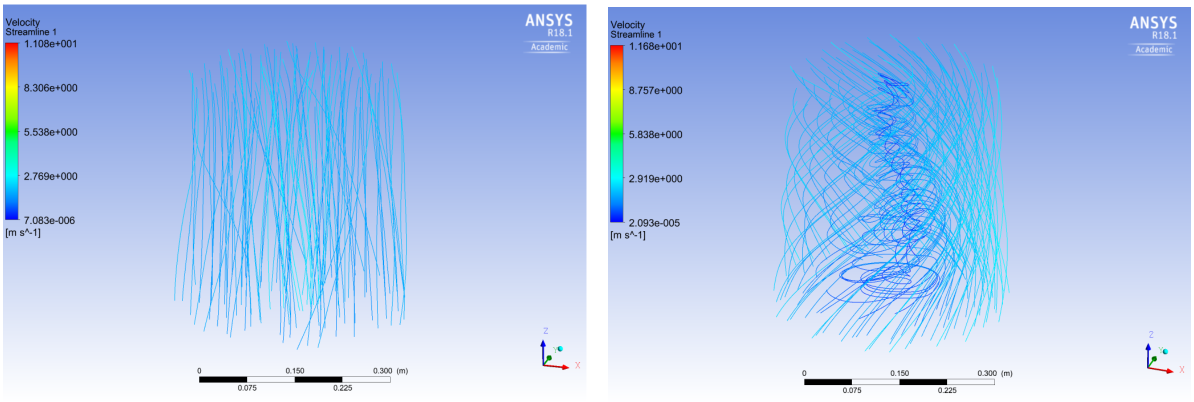

(a) α=9 degrees

(b) α=6 degrees

**Figure 7.** Velocity streamlines for α=9 degrees (a) and α=6 degrees (b) from the outlet of the runner to the outlet of the draft tube part. It is clear from the streamlines that there is a significant swirl component when the turbine is operating off-design.

### *4.2. Frequency analysis for BEP*

The frequencies obtained through simulations corresponded well with theory. This can be seen from figure 8. Frequency spectrums labelled relative frequencies are normalized as $f_{GV}/f_n=28$ and $f_{BP}/f_n=30$. The amplitudes in all the frequency spectra's have been normalized against the highest peak.

For all the monitor points in the runner, R1, R2 R3 and R4, the dominant frequency is $28{\cdot}f_n$, i.e. the guide vane passing frequency. It is apparent that the amplitude of the guide vane passing frequency is increasing when the distance from the guide vanes is decreasing. The monitor point in the vaneless space, VL01, showed a dominant frequency of $30{\cdot}f_n$, the blade passing frequency.

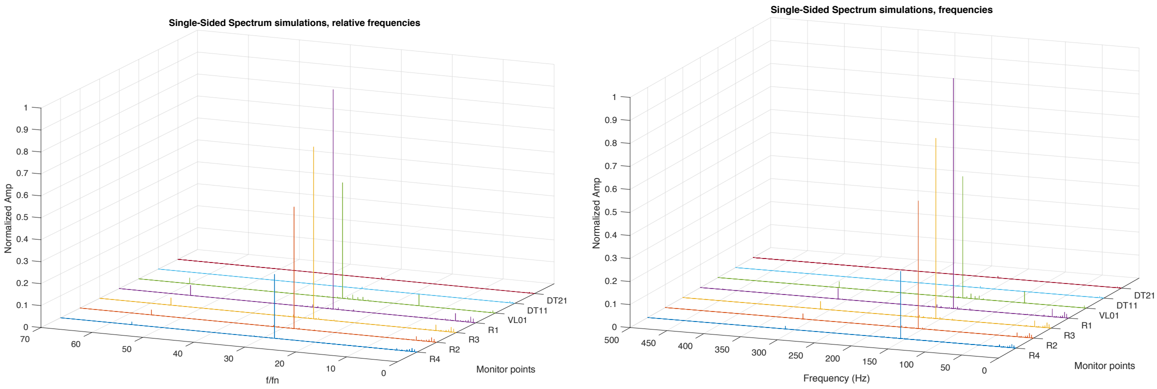

(a) (b)

**Figure 8.** Frequency spectrum obtained through CFD for BEP. Frequencies are relative to $f_n$ in a, while b shows the actual frequencies. Amplitudes are normalized against the highest peak.

The smaller peaks appearing at 56·$f_n$ for R1, R2, R3 and R4 is the second harmonic for the guide vane passing frequency, and it has a low amplitude. This coincides with the theory of Seidel et al. [10], that the higher harmonics are not that prominent. The second peak for VL01 appears at 60·$f_n$ and is the second harmonic of the blade passing frequency.

The blade passing frequency was observed in the draft tube as well. However, the relative amplitudes were very small compared to the relative amplitudes obtained at the monitor points in the vaneless space and runner that the effect is almost invisible. Figure 9 a shows the frequency of 30·$f_n$ for only the draft tube monitor points.

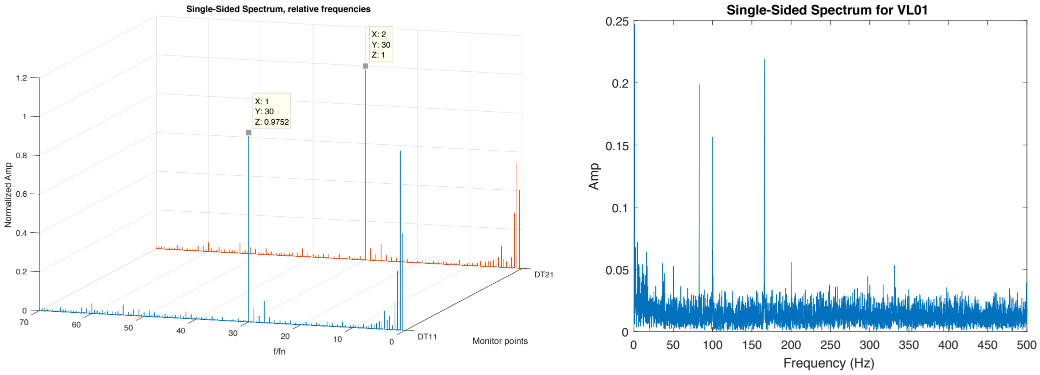

(a) (b)

**Figure 9.** The frequencies observed in the draft tube is shown in figure a . Figure b shows the unfiltered frequency spectrum for sensor VL01.

The frequency spectra for the experimental results are characterized by a lot of noise as can be seen from figure 11 b. The peaks observed at 50 Hz, 100 Hz, 200 Hz and 300 Hz are related to electrical power [22]. Because the RSI induced frequencies are what is investigated in this paper, a bandpass filter and bandstop filter has been utilized in order to remove noise and frequencies that are not of interest. The filters were generated using the built in filterBuilder in Matlab. The heavily filtered frequency spectra's from the experimental results are presented in figure 10. The amplitudes on the vertical scale are normalized to the highest peak.

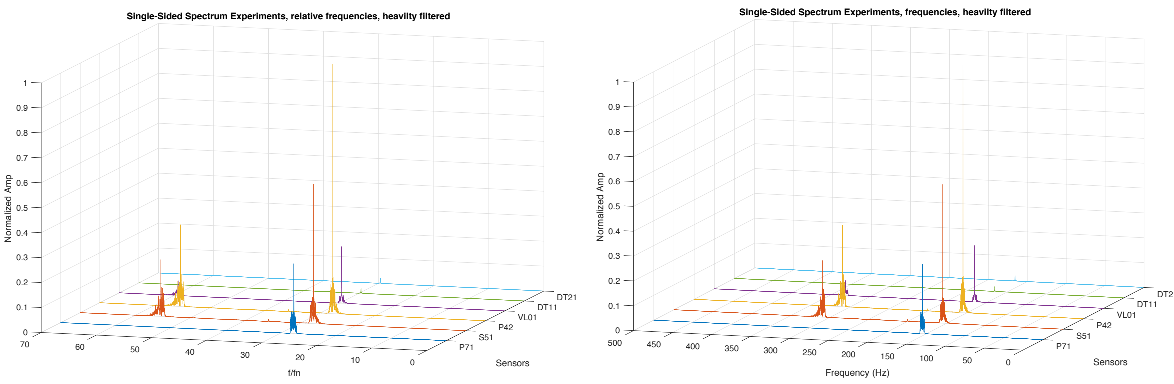

(a) (b)

**Figure 2.** The spectrum for all sensors. Frequency $f$ is relative to $f_n$. Amplitude in kPa.

### *4.3. Amplitudes at BEP*

While estimating the pressure peak-to-peak amplitudes for the experimental measurements requires using a Histrogram method or similar, the pressure curves from the simulations are periodic and the amplitude does not vary much. The approximate peak-to-peak amplitude was therefore calculated in Matlab by finding the peaks and troughs of the simulation pressure curves, then finding the mean peak value and the mean through value, before subtracting the mean trough from the mean peak. Amplitudes are presented in table 4.

| Location | R1 | R2 | R3 | R4 | VL01 | DT11 | DT21 |
|---|---|---|---|---|---|---|---|
| **Amplitude (kPa)** | 4.106 | 2.275 | 3.215 | 1.197 | 2.180 | 0.03144 | 0.03223 |

**Table 4.** Amplitudes (kPa) at different monitor point locations.

The tendency of decreasing amplitude in the runner as distance from the guide vanes is increasing is again observed in table 4. Bear in mind that R2 is actually placed further away from the guide vanes than R3.

## 5. Conclusion

The frequency spectras from the transient numerical analysis of BEP coincides well with theory and experimental measurements. The steady state results also agree with measurements, even though they deviate more further away from BEP. However, the results seem reasonable enough to use for further transient analyses.

Further work includes time step convergence test, steady state simulations for more operating points and transient simulations for all operating points. Transient simulations are going to be run on the supercomputer Vilje at NTNU. The numerical results are subsequently going to be compared to measurements, and a hill chart will be made based on simulations.

## References

[1] Anup KC, Bhola Thapa, and Young-Hoo Lee, "Transient numerical analysis of rotor-stator interaction in a Francis turbine," *Renewable Energy*, vol. 65, October 2013.

[2] Anup KC, Young-Ho Lee, and Bhola Thapa, "CFD study on prediction of vortex shedding in draft tube of Francis tubrine and vortex control techniques," *Renewable Energy*, no. 86, 2016.

[3] A. V. Minakov, D. V. Platonov, A. A. Dekterev, A. V. Sentyabov, and A. V. Zakharov, "The numerical simulation of low frequency pressure pulsations in the high-head Francis turbine," *Computers & Fluids*, vol. 111, February 2015.

[4] W. J. Rheingans, "Power Swings in Hydroelectric Power Plants," *Transactions of the A.S.M.E.*, vol. 62, no. 3, pp. 171-184, April 1940.

[5] Dragica Jošt and Andrej Lipej, "Numerical Prediction of Non-Cavitating and Cavitating Vortex Rope in a Francis Turbine Draft Tube," *Strojniski vestnik - Journal of Mechanical Engineering*, vol. 57, 2011.

[6] Christoph Nicolet, Nicolas Ruchonnet, and François Avellan, "One-Dimensional Modeling of Rotor Stator Interaction in Francis Pump-Turbine," *23rd IAHR Symposium - Yokohama*, October 2006.

[7] M V Magnoli and R Schilling, "Numerical simulation of pressure pulsations in Francis turbines," *IOP Conference Series: Earth and Environmental Science*, vol. 15, 2012.

[8] Hu Ying, Cheng Heming, Hu Ji, and Li Xirong, "Numerical simulation of unsteady turbulent flow through a Francis turbine," *Wuhan University Journal of Natural Sciences*, vol. 16, April 2011.

[9] Xiao Yexiang et al., "Numerical analysis of unsteady flow under high-head operating conditions in Francis turbine," *Engineering Computations: International Journal for Computer-Aided Engineering and Software*, vol. 27, no. 3, pp. 365-386, 2010.

[10] U. Seidel, B. Hübner, J. Löfflad, and P. Faigle, "Evaluation of RSI-induced stresses in Francis runners," *IOP Conference Series: Earth and Environmental Science*, no. 15, 2012.

[11] Chirag Trivedi, Michel Cervantes, and Ole Gunnar Dahlhaug, "Experimental and Numerical Studies of a High-Head Francis Turbine: A Review of the Francis-99 Test Case," *Energies*, January 2016.

[12] L. Meng, S. P. Zhang, L. J. Zhou, and Z. W. Wang, "Study in the Pressure Pulsation inside Runner with Splitter Blades in Ultra-High Head Turbine," *IOP Conference Series: Earth and Environmental Science*, vol. 22, 2014.

[13] Frank M. White, *Viscous Fluid Flow*, Third edition ed. New York, USA: McGraw-Hill Educations, 2006.

[14] Einar Kobro, "Measurement of Pressure Pulsations in Francis Turbines," EPT, NTNU, Trondheim, Doctoral thesis 2010.

[15] Torbjørn K. Nielsen, *Dynamic Dimensioning of Hydro Power Plants*.: NTNU, vol. 1990.

[16] sharcnet.ca. (2015, June) 5.4.3. GGI (General Grid Interface) Connections. [Online]. https://www.sharcnet.ca/Software/Ansys/16.2.3/en-us/help/cfx_mod/CACBCJBF.html

[17] sharcnet.ca. (2015) 5.3.3. General Connection. [Online]. https://www.sharcnet.ca/Software/Ansys/17.0/en-us/help/cfx_mod/CACDIGEH.html

[18] Zhao et al Yaping, "Performance study for Francis-99 by using different turbulence models," *Journal of Physics: Conference Series*, vol. 579, 2015.

[19] F. R. Menter, "Two-Equation Eddy-Viscosity Turbulence Models for Engineering Applications," *AIA A Journal*, vol. 32, no. 8, August 1994.

[20] Larry Hardesty. (2009, November) Explained: The Discrete Fourier Transform. [Online]. http://news.mit.edu/2009/explained-fourier

[21] G. Heinzel, A. Rüdiger, and R. Schilling, "Spectrum and spectral density estimation by the Discrete Fourier transform (DFT), including a comprehensive list of window functions and some flat-top windows," Teilinsitut, Max-Planck-Institut für Gravitationsphysik (Albert-Einstein-Institute), Hannover, Technical report 2002.

[22] NTNU. (2014) Norwegian Hydropower Centre. [Online]. https://www.ntnu.edu/nvks/experimental-study

[23] H. Wallimann and R. Neubauer, "Numerical Study of a High Head Francis Turbine with Measurements from the Francis-99 Project," *Journal of Physics: Conference Series*, vol. 579, 2015.

[24] J. D. Buron, S. Houde, R. Lestriez, and C. Deschênes, "Application of the non-linear harmonic method to study the rotor-stator interaction in Francis-99 yest case," *Journal of Physics: Conference Series*, vol. 579, 2015.

[25] Rahul Goyal and Bhupendra K. Gandhi, "Review of hydrodynamics instabilities in Francis turbine during off- design and transient operations," *Renewable Energy*, vol. 116, October 2017.

## Abbreviations

| | |
|---|---|
| CFD | Computational Fluid Dynamics |
| RSI | Rotor-Stator Interaction |
| BEP | Best Efficiency Point |
| DFT | Discrete Fourier Transform |
| FFT | Fast Fourier Transform |
| RMS | Root Mean Square |
| SAS-SST | Scale-Adaptive Simulation SST |
| SST | Shear Stress Transport |
| ZLES | Zonal Large Eddy Simulation |

## Symbols

| **Symbol** | **Description** | **Unit** |
|---|---|---|
| $A_{mn}$ | Combined pressure amplitude | Pa |
| $B_m$ | Amplitude for the $m^{th}$ harmonic | Pa |
| $B_n$ | Amplitude for the $n^{th}$ harmonit | Pa |
| $f_{BP}$ | Blade passing frequency | Hz |
| $f_{GV}$ | Guide vane passing frequency | Hz |
| $f_n$ | Runner rotation frequency | Hz |
| $f_R$ | Rheingan's frequency | Hz |
| $m$ | Harmonic order | |
| $n$ | Harmonic order | |
| $Z_{GV}$ | Number of guide vanes | |
| $Z_{BP}$ | Number of runner blades | |
| $Re$ | Reynolds number | |
| $\omega_b$ | Runner angular speed | rad/s |
| $\varphi$ | Discharge coefficient, $\varphi=Q/\pi\omega R_{ref}^2$ | |
| $\theta_s$ | Angle in stationary system | |
| $\theta_r$ | Angle in rotating system | |
| $\varphi_m$ | Phase for $m^{th}$ harmonic | |
| $\varphi_n$ | Phase for $n^{th}$ harmonic | |
| $\rho$ | Density | kg/m$^3$ |
| $\omega$ | Specific turbulence dissipation rate | 1/s |
| $F_1$ | Function | |
| $k$ | Turbulent kinetic energy | J/kg |
| $\beta^*$ | Closing constant | |
| $\beta_1$ | Closing constant | |
| $\mu$ | Dynamic viscosity | Ns/m$^2$ |
| $\mu_t$ | Turbulent viscosity | Ns/m$^2$ |
| $\sigma_k$ | Closing constant | |
| $\sigma_\omega$ | Closing constant | |
| $\sigma_{\omega1}$ | Closing constant | |
| $\sigma_{\omega2}$ | Closing constant | |
| $\nu_t$ | Eddy viscosity | m$^2$/s |
| $\gamma$ | $\gamma_1= \beta_1/ \beta^*-\sigma_{\omega1}\kappa^2/\mathrm{sqrt}(\beta^*)$ | |
| $\kappa$ | Closing constant | |
| $\tau$ | Turbulent shear stress | Pa |

# APPENDIX C: MATLAB scripts

This appendix contain the most important MATLAB scripts used in this thesis. The function for FFT below was created such that it could simply be called in any MATLAB script to perform a FFT on any signal.

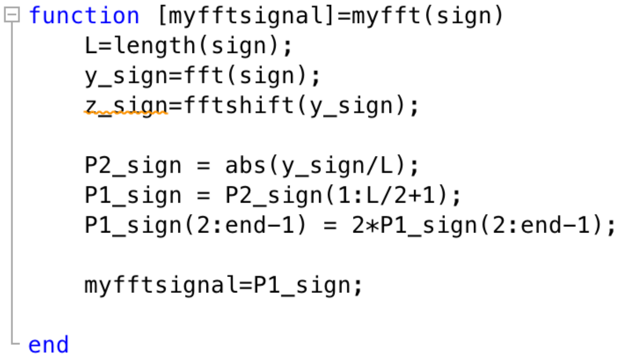

```
function [myfftsignal]=myfft(sign)
    L=length(sign);
    y_sign=fft(sign);
    z_sign=fftshift(y_sign);

    P2_sign = abs(y_sign/L);
    P1_sign = P2_sign(1:L/2+1);
    P1_sign(2:end-1) = 2*P1_sign(2:end-1);

    myfftsignal=P1_sign;

end
```

```
%Obtaining frequency spectrum for PTGV3 at all alphas


%Detrend all signals
S_GV3_1000 = detrend(GV3_1000(end-749:end));
S_GV3_1100 = detrend(GV3_1100(end-749:end));
S_GV3_1200 = detrend(GV3_1200(end-749:end));
S_GV3_1300 = detrend(GV3_1300(end-749:end));
S_GV3_1400 = detrend(GV3_1400(end-749:end));
S_GV3_400 = detrend(GV3_400(end-749:end));
S_GV3_500 = detrend(GV3_500(end-749:end));
S_GV3_600 = detrend(GV3_600(end-749:end));
S_GV3_700 = detrend(GV3_700(end-749:end));
S_GV3_800 = detrend(GV3_800(end-749:end));
S_GV3_900 = detrend(GV3_900(end-749:end));

%Repeats signal and filters out low frequencies
S_GV3_1000 = hipass_diffalpha_GV3(repmat(S_GV3_1000,27,1));
S_GV3_1100 = hipass_diffalpha_GV3(repmat(S_GV3_1100,27,1));
S_GV3_1200 = hipass_diffalpha_GV3(repmat(S_GV3_1200,27,1));
S_GV3_1300 = hipass_diffalpha_GV3(repmat(S_GV3_1300,27,1));
S_GV3_1400 = hipass_diffalpha_GV3(repmat(S_GV3_1400,27,1));
S_GV3_400 = hipass_diffalpha_GV3(repmat(S_GV3_400,27,1));
S_GV3_500 = hipass_diffalpha_GV3(repmat(S_GV3_500,27,1));
S_GV3_600 = hipass_diffalpha_GV3(repmat(S_GV3_600,27,1));
S_GV3_700 = hipass_diffalpha_GV3(repmat(S_GV3_700,27,1));
S_GV3_800 = hipass_diffalpha_GV3(repmat(S_GV3_800,27,1));
S_GV3_900 = hipass_diffalpha_GV3(repmat(S_GV3_900,27,1));


% %Defining timestep and length
dt = [0.0004706 0.00047267 0.0004741 0.0004743 0.0004757 0.0004762
 0.00047976 0.00047662 0.0004762 0.0004776 0.00047876] ; %timestep
n = [340. 338.5 337.5 337.3 336.3 336. 333.5 335.7 336. 335. 334.2];


s = length(dt);
Fs = zeros(s, 1);
fn = zeros(s, 1);
L=length(S_GV3_1000);


for i = 1:s
    Fs(i) = [1/dt(i)];
    fn(i) = [n(i)/60];
end


f4 = Fs(1)*((0:(L/2))/L);
f5 = Fs(2)*((0:(L/2))/L);
f6 = Fs(3)*((0:(L/2))/L);
f7 = Fs(4)*((0:(L/2))/L);
```

```
f8 = Fs(5)*((0:(L/2))/L);
f9 = Fs(6)*((0:(L/2))/L);
f10 = Fs(7)*((0:(L/2))/L);
f11 = Fs(8)*((0:(L/2))/L);
f12 = Fs(9)*((0:(L/2))/L);
f13 = Fs(10)*((0:(L/2))/L);
f14 = Fs(11)*((0:(L/2))/L);

fratio4 = f4/fn(1);
fratio5 = f5/fn(2);
fratio6 = f6/fn(3);
fratio7 = f7/fn(4);
fratio8 = f8/fn(5);
fratio9 = f9/fn(6);
fratio10 = f10/fn(7);
fratio11 = f11/fn(8);
fratio12 = f12/fn(9);
fratio13 = f13/fn(10);
fratio14 = f14/fn(11);




%FFT
s4=myfft(S_GV3_400);
s5=myfft(S_GV3_500);
s6=myfft(S_GV3_600);
s7=myfft(S_GV3_700);
s8=myfft(S_GV3_800);
s9=myfft(S_GV3_900);
s10=myfft(S_GV3_1000);
s11=myfft(S_GV3_1100);
s12=myfft(S_GV3_1200);
s13=myfft(S_GV3_1300);
s14=myfft(S_GV3_1400);

t4 = linspace(0,dt(1)*L,L); %time vector
t5 = linspace(0,dt(2)*L,L);
t6 = linspace(0,dt(3)*L,L);
t7 = linspace(0,dt(4)*L,L);
t8 = linspace(0,dt(5)*L,L);
t9 = linspace(0,dt(6)*L,L);
t10 = linspace(0,dt(7)*L,L);
t11 = linspace(0,dt(8)*L,L);
t12 = linspace(0,dt(9)*L,L);
t13 = linspace(0,dt(10)*L,L);
t14 = linspace(0,dt(11)*L,L);




%figures

a=1.951;
```

```
figure(3)
plot3(ones(1,length(f4)),fratio4,s14/1000/a)
hold on
plot3(2*ones(1,length(f4)),fratio5,s13/1000/a)
hold on
plot3(3*ones(1,length(f4)),fratio6,s12/1000/a)
hold on
plot3(4*ones(1,length(f4)),fratio7,s11/1000/a)
hold on
plot3(5*ones(1,length(f4)),fratio8,s10/1000/a)
hold on
plot3(6*ones(1,length(f4)),fratio9,s9/1000/a)
hold on
plot3(7*ones(1,length(f4)),fratio10,s8/1000/a)
hold on
plot3(8*ones(1, length(f4)),fratio11,s7/1000/a)
hold on
plot3(9*ones(1, length(f4)),fratio12,s6/1000/a)
hold on
plot3(10*ones(1, length(f4)),fratio13,s5/1000/a)
hold on
plot3(11*ones(1, length(f4)),fratio14,s4/1000/a)
title('Single-Sided Spectrum, Simulations at location GV3')
ylabel('Normalized Frequency, \it f/f_n \rm [-]')
zlabel('Relative Amplitude [-]')
ylim([0,80])
xlim([0,12])
zlim([0,1.001])
xlabel('Guide vane opening, \alpha [°]')
xticks([1 2 3 4 5 6 7 8 9 10 11 12 13 14])
xticklabels({'14','13','12','11','10','9','8','7','6','5','4'})
%xtickangle(-20)
%set(gca,'Ydir','reverse')
set(gca,'fontsize',18)
view([105,60,30])
grid on
```

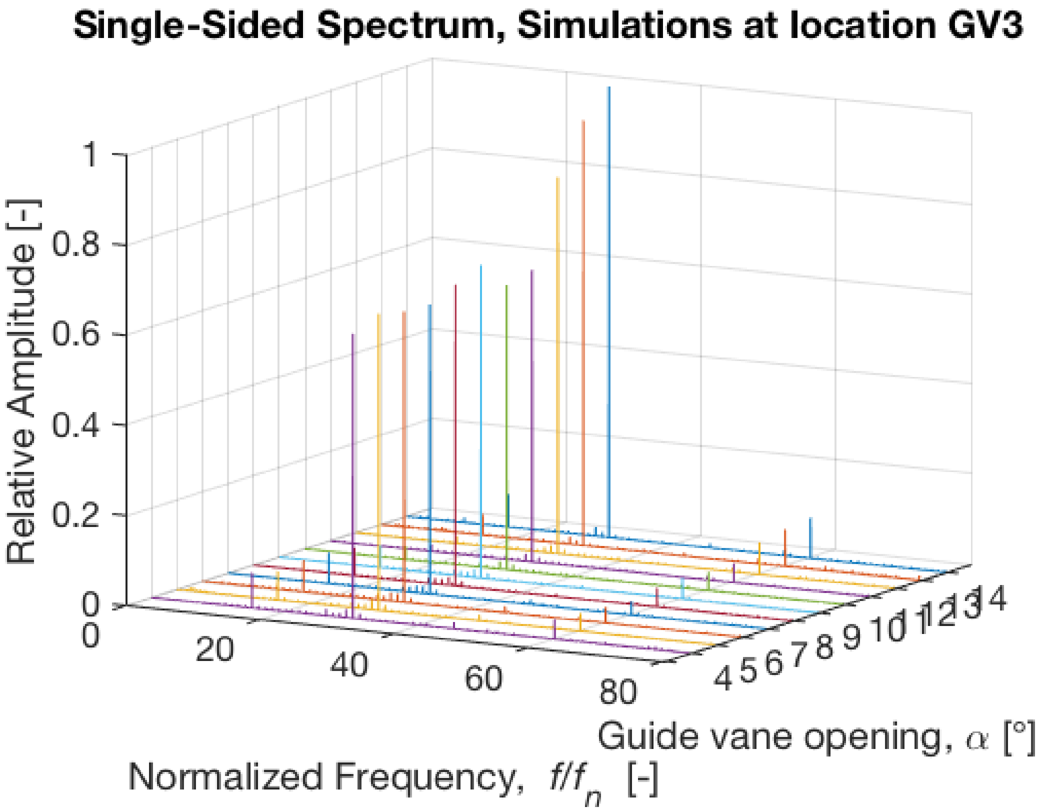

*Published with MATLAB® R2017b*

```
%Obtaining frequency spectrum for different monitor point at constant
 alpha


%Detrend all signals
S_PTR2 = detrend(PTR2(end-749:end));
S_PTR3 = detrend(PTR3(end-749:end));
S_PTR4 = detrend(PTR4(end-749:end));

S_GV1 = detrend(GV1(end-749:end));
S_GV3 = detrend(GV3(end-749:end));
S_GV4 = detrend(GV4(end-749:end));

%Repeats signal
S_PTR2 = repmat(S_PTR2,27,1);
S_PTR3 = repmat(S_PTR3,27,1);
S_PTR4 = repmat(S_PTR4,27,1);

S_GV1 = repmat(S_GV1,27,1);
S_GV3 = repmat(S_GV3,27,1);
S_GV4 = repmat(S_GV4,27,1);

% %Defining timestep and length

dt = [0.0004706 0.00047267 0.0004741 0.0004743 0.0004757 0.0004762
 0.00047976 0.00047662 0.0004762 0.0004776 0.00047876] ; %timestep
n = [340. 338.5 337.5 337.3 336.3 336. 333.5 335.7 336. 335. 334.2];


s = length(dt);
Fs = zeros(s, 1);
fn = zeros(s, 1);
L=length(S_GV3);


for i = 1:s
    Fs(i) = [1/dt(i)];
    fn(i) = [n(i)/60];
end

f4 = Fs(1)*((0:(L/2))/L);
f5 = Fs(2)*((0:(L/2))/L);
f6 = Fs(3)*((0:(L/2))/L);
f7 = Fs(4)*((0:(L/2))/L);
f8 = Fs(5)*((0:(L/2))/L);
f9 = Fs(6)*((0:(L/2))/L);
f10 = Fs(7)*((0:(L/2))/L);
f11 = Fs(8)*((0:(L/2))/L);
f12 = Fs(9)*((0:(L/2))/L);
f13 = Fs(10)*((0:(L/2))/L);
f14 = Fs(11)*((0:(L/2))/L);
```

```
fratio4 = f4/fn(1);
fratio5 = f5/fn(2);
fratio6 = f6/fn(3);
fratio7 = f7/fn(4);
fratio8 = f8/fn(5);
fratio9 = f9/fn(6);
fratio10 = f10/fn(7);
fratio11 = f11/fn(8);
fratio12 = f12/fn(9);
fratio13 = f13/fn(10);
fratio14 = f14/fn(11);

%FFT
sPTR2=myfft(S_PTR2);
sPTR3=myfft(S_PTR3);
sPTR4=myfft(S_PTR4);


sGV1=myfft(S_GV1);
%sGV2=myfft(S_GV2);
sGV3=myfft(S_GV3);
sGV4=myfft(S_GV4);

%figures

a=1.672;

figure(3)
plot3(ones(1,length(f4)),fratio4,sGV4/1000/a)
hold on
plot3(2*ones(1, length(f4)),fratio4,sGV3/1000/a)
hold on
plot3(3*ones(1, length(f4)),fratio4,sGV1/1000/a)
hold on
plot3(4*ones(1, length(f4)),fratio4,sPTR4/1000/a)
hold on
plot3(5*ones(1, length(f4)),fratio4,sPTR3/1000/a)
hold on
plot3(6*ones(1, length(f4)),fratio4,sPTR2/1000/a)
title('Single-Sided Spectrum, Simulations at \alpha=4°')
ylabel('Normalized Frequency, \it f/f_n \rm [-]')
zlabel('Relative Amplitude [-]')
xlim([0,7])
ylim([0,80])
zlim([0,1.001])
xtickangle(-20)
%set(gca,'Ydir','reverse')
set(gca,'fontsize',18)
xlabel('Monitor points')
view([120,50,40])
xticks([1 2 3 4 5 6])
xticklabels({'PTGV4','PTGV3','PTGV1','PTR4','PTR3','PTR2'})
grid on
```

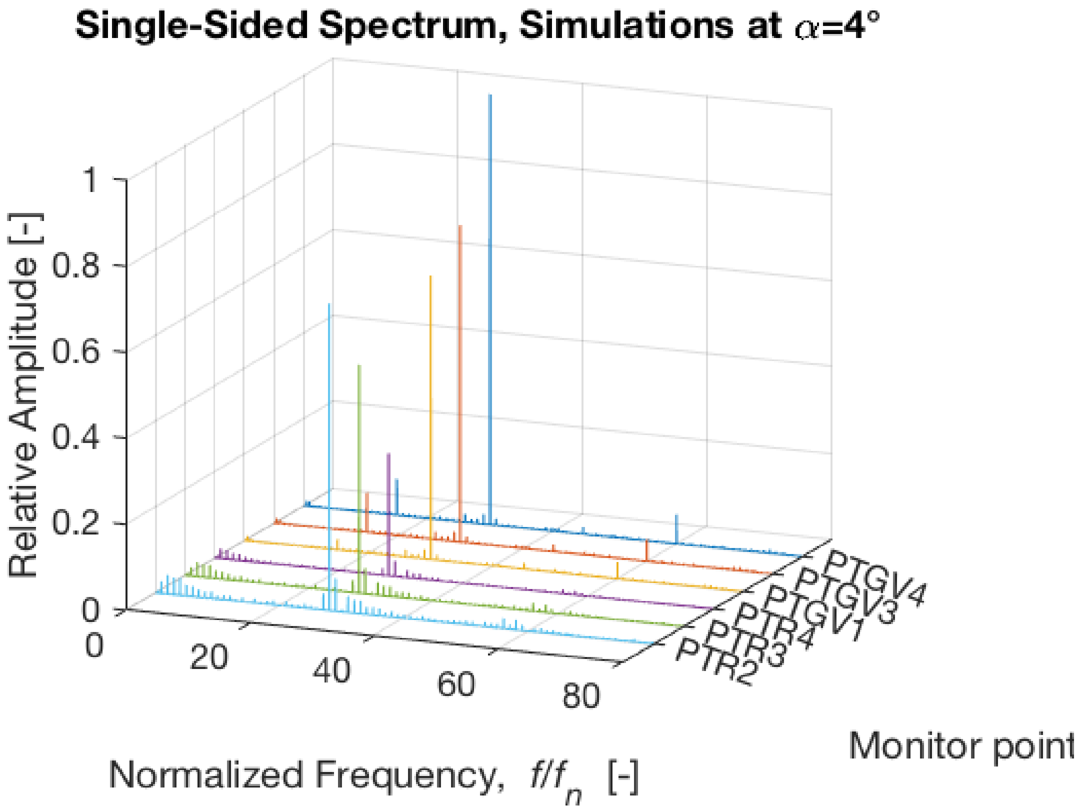

*Published with MATLAB® R2017b*